WIND
ENERGY
SCIENCE

Unsupervised anomaly detection of permanent-magnet offshore wind generators through electrical and electromagnetic measurements

Ali Dibaj[1], **Mostafa Valavi**[2], and **Amir R. Nejad**[1]

[1]Department of Marine Technology, Norwegian University of Science and Technology (NTNU),
Trondheim, Norway
[2]EDRMedeso AS, Oslo, Norway

Correspondence: Ali Dibaj (ali.dibaj@ntnu.no)

Abstract. This paper investigates fault detection in offshore wind permanent-magnet synchronous generators (PMSGs) for demagnetization and eccentricity faults (both static and dynamic) at various severity levels. The study utilizes a high-speed PMSG model on the National Renewable Energy Laboratory (NREL) 5 MW reference offshore wind turbine at the rated wind speed to simulate healthy and faulty conditions. An unsupervised convolutional autoencoder (CAE) model, trained on simulated signals from the generator in its healthy state, serves for anomaly detection. The main aim of the paper is to evaluate the possibility of fault detection by means of high-resolution electrical and electromagnetic signals, given that the typically low-resolution standard measurements used in supervisory control and data acquisition (SCADA) systems of wind turbines often impede the early detection of incipient failures. Signals analyzed include three-phase currents, induced shaft voltage, electromagnetic torque, and magnetic flux (air gap and stray) from different directions and positions. The performance of CAE models is compared across time and frequency domains. Results show that in the time domain, stator three-phase currents effectively detect faults. In the frequency domain, stray flux measurements, positioned at the top, bottom, and sides of the outside of the stator housing, demonstrate superior performance in fault detection and sensitivity to fault severity levels. In particular, radial components of stray flux can successfully distinguish between eccentricity and demagnetization.

1 Introduction

Permanent-magnet synchronous generators (PMSGs) have become popular recently in offshore wind applications driven by advancements in permanent-magnet materials and high-efficiency power electronics. Figure 1, sourced from the Global Offshore Wind Report 2022 (GWEC, 2022), illustrates the evolution of drivetrain technologies in offshore wind turbines within the European and Chinese markets from 2016 to 2021. The data indicate that in 2016 the market share of PMSGs was approximately 60 % in Europe and 10 % in China. By 2021, these shares had risen significantly, with PMSGs accounting for 100 % of the market share in Europe and 80 % in China.

Distinct from traditional doubly fed induction generators (DFIGs), PMSGs leverage permanent magnets to generate the magnetic field, thereby eliminating the need for a separate excitation system. This design eliminates components like slip rings and brushes, leading to higher reliability and reducing maintenance requirements. Available in both medium-speed and direct-drive configurations, these generators offer higher power density and efficiency, with added benefits such as improved grid stability because of a faster response to wind speed changes (Moghadam and Nejad, 2020; Freire and Cardoso, 2021; Carroll et al., 2015). However, despite their increased reliability, PMSGs are not completely immune to faults and have their own challenges, particularly in harsh offshore environments. Consequently, reliable con-
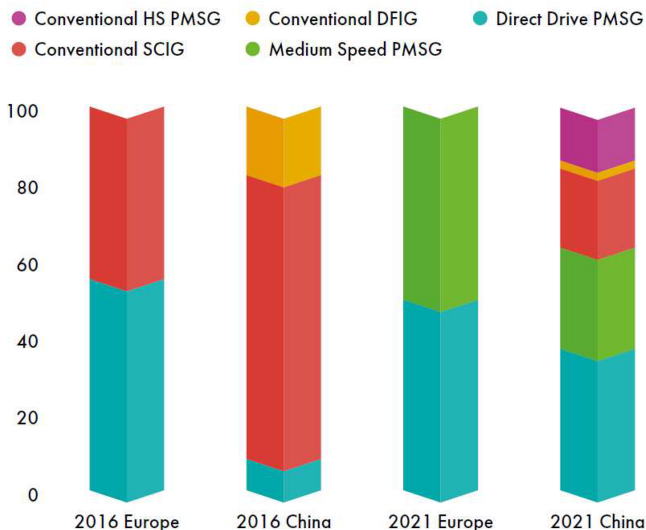
Figure 1. Trend of offshore wind turbine drivetrain technology between 2016 and 2021 (GWEC, 2022). HS: high speed; SCIG: squirrel-cage induction generator.

dition monitoring and early fault detection are essential to minimize production loss and prevent unexpected downtime in these machines (Nejad et al., 2022; Huang et al., 2023; Yang, 2009; Mahmoud et al., 2024).

PM machines, in general, are susceptible to several types of faults that can impact their functionality (Choi et al., 2018; Kudelina et al., 2021). Stator failures are common, which can include insulation faults and issues with the connections in the stator windings (Wang et al., 2014; Nyanteh et al., 2013; Hoang Nguyen et al., 2023; Ortiz-Medina et al., 2023). Air gap eccentricity can cause operational disturbances such as vibrations and noise and may lead to mechanical stress and uneven wear (Valavi et al., 2013; Ebrahimi et al., 2009, 2014; Tong et al., 2020). Demagnetization of the permanent magnets is also a critical fault, often triggered by excessive heat, leading to a permanent reduction in the generator's efficiency and power output (Faiz and Mazaheri-Tehrani, 2017; Huang et al., 2023; Ebrahimi et al., 2022; Wang et al., 2016). Additionally, failures in the cooling and control systems can significantly impact the PMSG's performance (Borchersen and Kinnaert, 2016). The cooling system is crucial for maintaining an optimal operational temperature and preventing overheating, while the control system manages the generator's operational parameters (Freire and Cardoso, 2021).

This study examines the problems of demagnetization and eccentricity failures which are commonly encountered in PMSGs. Currently, there is a lack of established techniques to effectively address these issues and meet the requirements of the wind sector. The demagnetization issue is exacerbated in offshore environments where thermal management is more difficult due to excessive humidity, maintenance, and accessibility concerns (Gyftakis et al., 2023). Demagnetization in

PMSGs can be either local or distributed, each showing distinct fault signatures. Local demagnetization refers to the loss of magnetic properties in specific areas of the magnetic poles, often due to localized overheating or physical damage. Distributed demagnetization, on the other hand, involves a uniform reduction in magnetic strength across the entire magnet, typically resulting from prolonged exposure to high temperatures or electrical faults (Choi et al., 2018; Choi, 2021). Eccentricity is also characterized as static and dynamic. Static eccentricity is characterized by a constant offset between the rotor and stator, leading to an uneven magnetic field and potentially causing vibrations and wear. Dynamic eccentricity involves a varying distance between the rotor and stator during rotation, which can result in fluctuating magnetic forces, additional stress on bearings, and operational instability (Freire and Cardoso, 2021; Kudelina et al., 2021).

Various monitoring techniques are employed for the purpose of condition monitoring and fault detection of electrical machines, including PMSGs, depending on the specific type of failure. Vibration analysis, which commonly utilizes high-resolution accelerometer data (Dibaj et al., 2022, 2023), is performed to identify defects such as mechanical unbalance and bearing damage (Ágoston, 2015; Ali et al., 2019; Ding et al., 2022), eccentricity (Ogidi et al., 2015; Su and Chong, 2007), and electrical faults (Singh and Sa'ad Ahmed, 2004; Su et al., 2011). However, early-stage electrical and electromagnetic faults do not often produce significant mechanical vibrations and, therefore, are not easily detectable from vibration signatures. Temperature monitoring techniques such as supervisory control and data acquisition (SCADA) systems (Zhao et al., 2017; Qiu et al., 2016) or infrared thermography (Stipetic et al., 2012; Lopez-Perez and Antonino-Daviu, 2017) can detect problems related to bearings (Choudhary et al., 2021), short circuits in stator coils (Khanjani and Ezoji, 2021), and cooling systems (Borchersen and Kinnaert, 2016). However, temperature-based methods face challenges, including difficulty in placing a sensor to accurately identify specific faults; the sensor's general sensitivity that might only offer a broad temperature overview rather than detailed hotspots; and the potential influence of environmental conditions on temperature readings, which may affect the precise identification of problems. Furthermore, temperature measurements, as a part of SCADA systems, are unable to capture fast dynamics and provide fault discrimination at the required level because of low-resolution data.

In this work, electrical and electromagnetic signals, including stator phase currents, induced shaft voltage, electromagnetic torque, and magnetic flux density inside and outside the air gap, are analyzed and compared for fault detection in PMSGs. Harmonic analysis of electrical and electromagnetic signals is a common technique for identifying faults in PM machines across various industries and applications, as supported by various studies (Valavi et al., 2018, 2013; Bernier et al., 2023;

Da et al., 2013; Zhang et al., 2021). Furthermore, advanced signal processing methods such as wavelet transform (Ehya et al., 2022a) and Hilbert–Huang transform (Zhang et al., 2021) are also used to extract harmonic characteristics from these signals. Despite these approaches, the effectiveness of these measurements, particularly the electromagnetic ones, in providing early failure warnings in large MW-scale (megawatt-scale) offshore PMSGs has yet to be established. Additionally, it is important to note that certain measurements examined in this work, such as phase currents, might also be integrated into the SCADA systems of wind turbines. However, the raw data of these measurements are typically downsampled in SCADA systems to a 10 min resolution. The main drawback of the downsampled data of SCADA systems is that they cannot pinpoint incipient failures in PMSGs as early as possible, highlighting an essential area for research on the capabilities of these measurements.

Recent advancements in computational power and cloud computing have significantly shifted industrial asset management towards machine learning and artificial intelligence techniques (Peres et al., 2020; Lei et al., 2020). This shift aims to address the inefficiencies of traditional data management methods in handling the vast amounts of data involved in large-scale applications like offshore wind farms. Moreover, machine learning models are known for their scalability and flexibility (Lu et al., 2024). They do not have the limitation of traditional methods in maintaining accuracy as the scale of data and model complexity increases. Hoang Nguyen et al. (2023) implemented a gradient-boosting machine for detecting inter-turn short-circuit faults and local demagnetization using current and stray flux measurements. Cai et al. (2021) utilized vibration and acoustic emission data with a combined complementary ensemble empirical mode decomposition and Bayesian network model for fault detection in rolling element bearings. Huang et al. (2023) developed a semi-supervised rule-based classifier for demagnetization fault diagnosis, while Tan et al. (2020) explored the use of current measurements combined with an artificial neural network (ANN) for detecting faults in converter systems of PMSGs. Penrose (2022) investigated the application of the k-nearest neighbor (KNN) model for fault classification and linear regression models for estimating remaining useful life (RUL), providing a 30 d advance notification of failures in small electric machines using basic data inputs. Ehya et al. (2022b) examined different machine learning and signal processing techniques for diagnosing inter-turn short-circuit faults in salient-pole synchronous generators. Despite these advances, the application of machine learning for fault detection in MW-scale wind PMSGs is still largely unexplored (Freire and Cardoso, 2021).

Therefore, this study adopts a machine learning model for unsupervised anomaly detection, trained on collected simulated measurements in the healthy state. Unlike supervised learning, which requires a significant amount of labeled data with predefined class labels for training, unsupervised learning does not rely on labeled data. This characteristic is particularly beneficial in offshore wind applications, where acquiring extensive labeled fault-related data is challenging. Moreover, supervised learning methods often struggle to generalize to unseen fault scenarios. Consequently, a convolutional autoencoder (CAE) model is utilized, known for its capability to process complex and high-dimensional data efficiently.

In summary, this study aims to conduct a comparative analysis of different measurements – three-phase currents, induced shaft voltage, electromagnetic torque, and air gap and stray magnetic flux density – for the purpose of wind turbine PMSG anomaly detection using a CAE model. As mentioned earlier, despite the potential availability of a few of these measurements in SCADA systems, they are often recorded at a low resolution, typically every 10 min. The primary focus of this work is to explore the effectiveness of high-resolution measurements for the early detection of potential failures. The sensitivity of these measurements against the studied fault cases, including demagnetization and static and dynamic eccentricity at various levels of fault severity, will be analyzed. Simulated measurements will be collected from a simulation high-speed PMSG, designed and modeled based on the specifications of the National Renewable Energy Laboratory (NREL) 5 MW reference offshore wind turbine (Jonkman et al., 2009), tailored for offshore wind applications.

The remainder of the paper is structured as follows. Section 2 describes the generator model, measurements, and studied fault cases. Section 3 discusses the anomaly detection methodology employed in this study, including the CAE model, threshold determination, and performance metrics. Section 4 contains the results and discussion. Finally, the conclusion is outlined in Sect. 5.
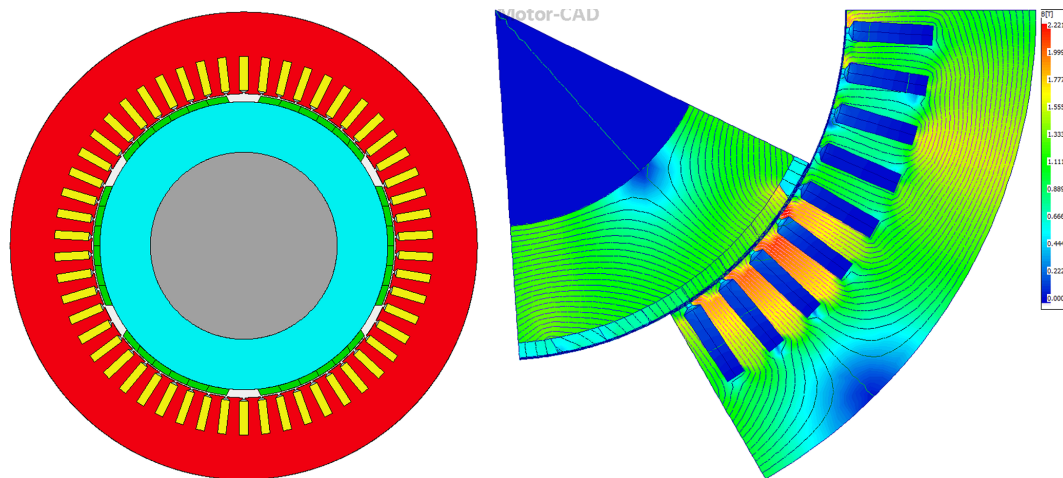
2 Generator model

A wind generator was designed according to the specifications and requirements detailed in "Definition of a 5-MW Reference Wind Turbine for Offshore System Development," a technical report published by the National Renewable Energy Laboratory (NREL) (Jonkman et al., 2009). Table 1 presents the drivetrain specifications as outlined in the report.

Following these specifications, a high-speed PMSG was developed and optimized. Figure 2 illustrates the two-dimensional cross-section of the designed PMSG along with its magnetic-field distribution. The analysis of the generator's performance was conducted using Ansys Motor-CAD, a specialized piece of software for electrical machine design. The generator features a surface-mounted permanent-magnet configuration with 6 poles and 54 slots. To minimize eddy current losses, the permanent-magnet blocks are segmented both radially and axially, which enhances efficiency and reduces the risk of demagnetization.

Table 1. Drivetrain specification (Jonkman et al., 2009).

Parameter	Value
Rated rotor speed (rpm)	12.1
Rated generator speed (rpm)	1173.7
Gearbox ratio	1 : 97
Electrical generator efficiency (%)	94.4
Generator inertia about high-speed shaft ($kg\,m^2$)	534.116
Equivalent driveshaft torsional-spring constant ($kN\,m\,rad^{-1}$)	867 637
Equivalent driveshaft torsional-damping constant ($kN\,m\,s\,rad^{-1}$)	6215
Fully deployed high-speed shaft brake torque ($N\,m$)	28116.2
High-speed shaft brake time constant (s)	0.6

Figure 2. Radial cross-section and magnetic-field distribution of the generator.

The wind generator is capable of producing 5.177 MW of electromagnetic power at the rated speed, achieving an efficiency of 98.74 %. The line current and voltage are measured at 1092 Arms (root mean square current) and 3184 Vrms (root mean square voltage), respectively. A performance analysis confirms that the generator meets the target power output with exceptional efficiency.

2.1 Measurements

In this study, a collection of simulated measurements from the PMSG model, as detailed in Table 2, are used in the anomaly detection task aimed at identifying fault cases outlined in Sect. 2.2. This set of collected data includes high-resolution induced shaft voltage; electromagnetic torque; stator phase currents; and air gap and stray magnetic flux, including both radial and tangential components at various positions. Variations observed in these measurements can indicate different types of faults depending on the symptoms manifested in the signal. For instance, flux sensors provide insights into the behavior of the magnetic field. Faults that introduce imbalances or irregularities to the rotating magnetic field can be identified using these sensors. Flux monitoring

has become popular recently thanks to advancements in sensor technology and low-cost and compact flux sensors such as search coils and Hall effect sensors (Mazaheri-Tehrani and Faiz, 2022). Figure 3 indicates the position of flux sensors implemented in the simulation model in this study. Also, Fig. 4 shows some examples of the time-domain waveform of simulated signals. As explained earlier, the motivation of this study extends to comparing the performance of the anomaly detection model trained with these simulated high-resolution signals to examine the diagnostic capabilities of each measurement type.

2.2 Fault cases

Two main categories of faults in the PMSG model are considered: partial demagnetization and eccentricity, which includes both static and dynamic forms. The investigation is of a series of fault cases within these categories. The aim is to evaluate the performance of anomaly detection method in varying degrees of fault severity using different measurement variables.

Partial demagnetization faults, outlined in Table 3, are explored through six distinct scenarios, each simulating varying

Table 2. Simulated electrical and electromagnetic measurements.

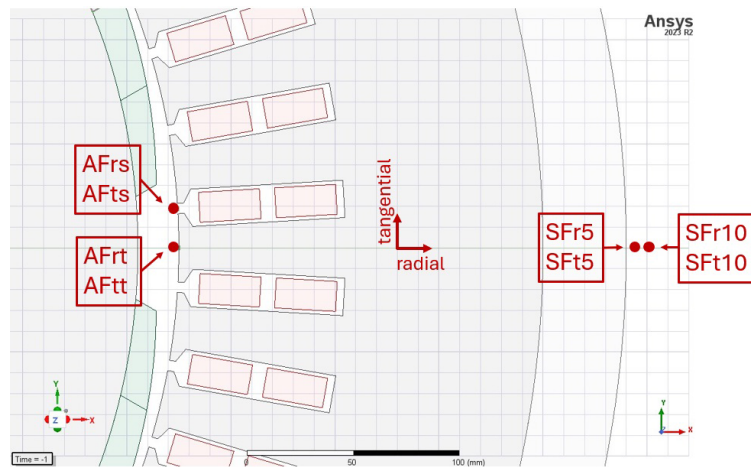|	Measurement
Vsh	Induced shaft voltage
Te	Electromagnetic torque
Is	Stator three-phase currents (three signals)
SFr5	Stray flux sensor – radial component, outside stator housing with a distance of 5 mm (top, bottom, and side locations – four signals)
SFt5	Stray flux sensor – tangential component, outside stator housing with a distance of 5 mm (top, bottom, and side locations – four signals)
SFr10	Stray flux sensor – radial component, outside stator housing with a distance of 10 mm (top, bottom, and side locations – four signals)
SFt10	Stray flux sensor – tangential component, outside stator housing with a distance of 10 mm (top, bottom, and side locations – four signals)
AFrt	Air gap flux sensor – radial component at tooth position (top, bottom, and side locations – four signals)
AFtt	Air gap flux sensor – tangential component at tooth position (top, bottom, and side locations – four signals)
AFrs	Air gap flux sensor – radial component at slot position (top, bottom, and side locations – four signals)
AFts	Air gap flux sensor – tangential component at slot position (top, bottom, and side locations – four signals)

Figure 3. Position of the flux sensors in the simulation wind PM generator model.

Table 3. Partial demagnetization with six cases.

	Fault description
Fault case 1 (FC1)	All segments of one pole (10 %)
Fault case 2 (FC2)	All segments of one pole (20 %)
Fault case 3 (FC3)	Two segments of one pole (40 % and 20 %)
Fault case 4 (FC4)	Two segments of one pole (80 % and 40 %)
Fault case 5 (FC5)	Two segments of all poles (20 % and 10 %)
Fault case 6 (FC6)	Two segments of all poles (40 % and 20 %)

levels of magnetic flux density reduction across the generator's permanent magnets. The first and second cases, FC1 and FC2, model a mild uniform 10 % and 20 % demagnetization affecting all segments of a single pole. FC3 and FC4 model more localized demagnetization, where only two segments of a single pole are demagnetized at different severities, 40 % and 20 % for FC3 and 80 % and 40 % for FC4, respectively. FC5 and FC6 extend this localized demagnetization to multiple poles, with two segments of all poles undergoing demagnetization at 20 % and 10 % for FC5 and 40 % and 20 % for FC6, respectively.
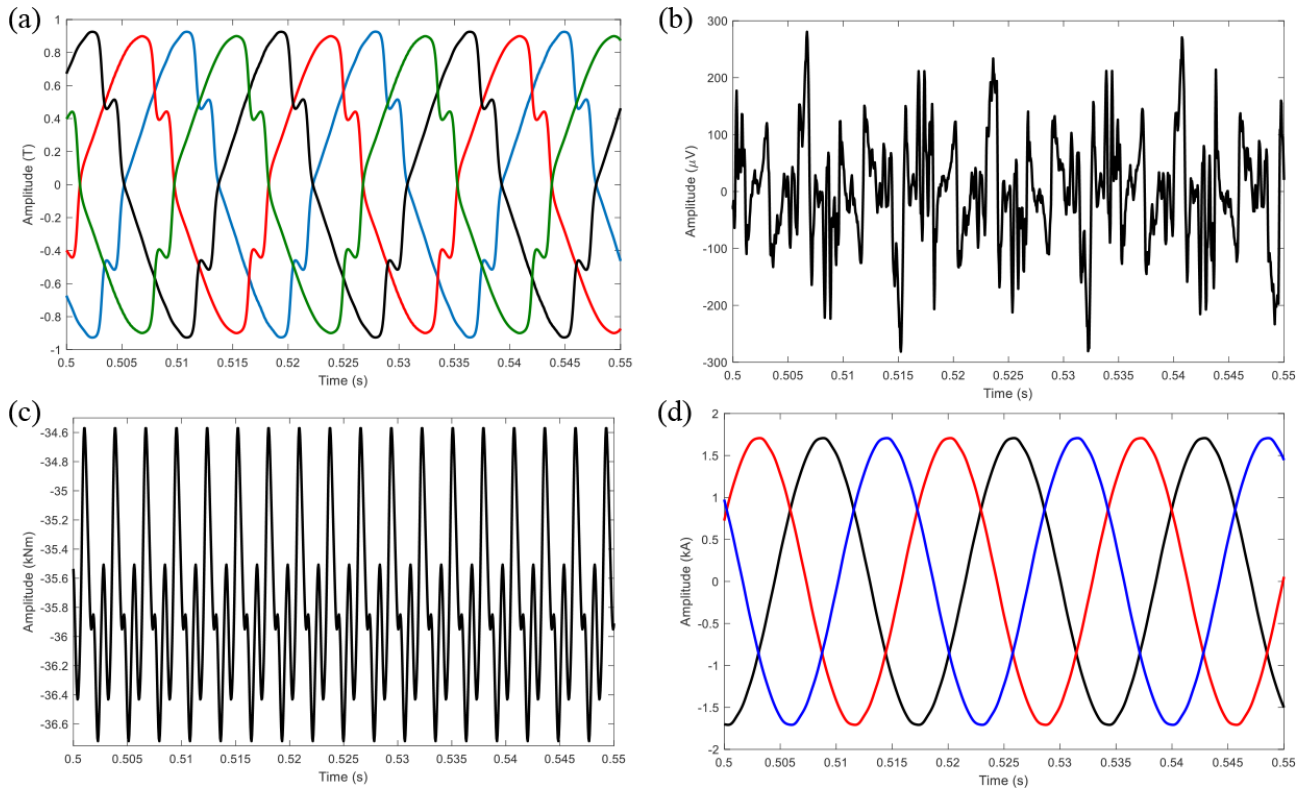
Figure 4. Time-domain waveform of the simulated data: **(a)** radial components of air gap flux (top, bottom, and side locations), **(b)** induced shaft voltage, **(c)** electromagnetic torque, and **(d)** stator three-phase currents. T: tesla; μV: microvolt.

Table 4. Static (SE) and dynamic (DE) eccentricity with six different degrees.

	Fault description
Fault case 1 (FC1)	Dynamic (5 %)
Fault case 2 (FC2)	Dynamic (15 %)
Fault case 3 (FC3)	Dynamic (25 %)
Fault case 4 (FC4)	Static (5 %)
Fault case 5 (FC5)	Static (15 %)
Fault case 6 (FC6)	Static (25 %)

Eccentricity, characterized by the misalignment of the rotor relative to the stator in the two-dimensional $(x-y)$ plane, is assessed through static and dynamic conditions across six cases as shown in Table 4. Dynamic eccentricity, from FC1 to FC3, addresses a variable misalignment where the rotor's axis orbits around the stator's axis at severities of 5 %, 15 %, and 25 %, respectively. Conversely, static eccentricity cases, FC4 to FC6, examine the impact of a fixed rotor offset from the stator axis, also at severities of 5 %, 15 %, and 25 %, respectively. The degree of eccentricity is quantified by the offset value of the shifted axis relative to the air gap length in the healthy condition.

3 Methodology

3.1 Convolutional autoencoders

Autoencoders (AEs), developed originally as neural network models for copying input to output, have significantly evolved to play a crucial role in unsupervised learning, dimensionality reduction, and data denoising (Goodfellow et al., 2016). In anomaly detection, AEs are particularly effective; they are trained on normal data to learn its representation, and anomalies are identified based on the higher reconstruction error when the model encounters data that deviate from this learned normal behavior. This higher reconstruction error is because the AE, trained on normal or healthy data, finds it challenging to reconstruct these new or deviant patterns. As mentioned previously, the unsupervised approach is advantageous in anomaly detection in wind turbine applications where anomalies are rare and often not labeled.

A typical AE consists of two main parts: the encoder and the decoder. The encoder compresses the input data as a sequence of data points $x = [x_1, x_2, x_3, \ldots, x_n]$ into a lower-dimensional representation known as feature space $h = [h_1, h_2, h_3, \ldots, h_d]$ $(d < n)$, and the decoder reconstructs the data back to its original form $\hat{x} = [\hat{x}_1, \hat{x}_2, \hat{x}_3, \ldots, \hat{x}_n]$ from this compressed representation as shown in Fig. 5. The for-
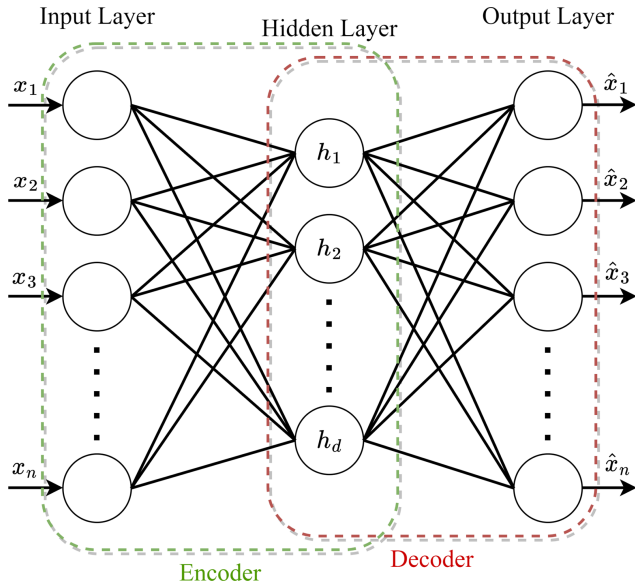
Figure 5. Typical autoencoder architecture.

mulation for a single-layer encoder and a single-layer decoder is described as follows:

$$h = f(x) = s(\mathbf{W}^1 x + \boldsymbol{b}^1), \tag{1}$$

$$\hat{x} = f(h) = s(\mathbf{W}^2 h + \boldsymbol{b}^2), \tag{2}$$

where $\mathbf{W}^1$ and $\mathbf{W}^2$ are weight matrices; $\boldsymbol{b}^1$ and $\boldsymbol{b}^2$ are bias vectors; and $s(.)$ is the activation function, which is commonly a Sigmoid function $\sigma(t) = 1/(1 + e^{-t})$ or a rectified linear unit function $\mathrm{ReLU}(t) = \max(0, t)$ for the encoder and decoder parts. For the output layer, this function can be a Sigmoid or a linear function, depending on the type of input data (Wu et al., 2021). The architecture of AE is adaptable, allowing for the modification of the number and size of its hidden layers to suit the complexity of the input data (Li et al., 2021). Given a set of training data $\{x^{(i)}\}_{i=1}^{N}$, the AE model is typically trained by minimizing the cost function J, often measured by mean squared error (MSE), through the backpropagation algorithm (Rumelhart et al., 1986), expressed as

$$J_{\mathrm{MSE}}(\mathbf{W}, \boldsymbol{b}) = \frac{1}{N} \sum_{i=1}^{N} \left\| \mathbf{x}_i - \hat{\mathbf{x}}_i \right\|^2. \tag{3}$$

This study employs multi-variable measurements like magnetic flux density measured at different angles. For such data, a standard one-dimensional AE will not work. In addition, the typical feed-forward AE does not take into account the spatial structure of data, therefore reducing the accuracy of the reconstruction process. To solve this, the convolutional autoencoder (CAE) model is used in this study. The CAE uses convolutional and deconvolutional layers instead of the fully connected layers found in the regular feed-forward autoencoder, as shown in Fig. 6.

The first part of the CAE works by compressing the data using a series of steps that involve convolution and pooling. The convolution layers perform operations that apply a filter to the input, which helps to capture important parts of the data depending on the filter used. After each convolution layer, a pooling step follows. This step usually uses a max-pooling layer, which reduces the size of the output from the convolution by picking the highest value from each segment of the input data covered by the filter. The second part of the CAE is about decoding the features that the first part extracted. This is done with deconvolutional layers. These layers increase the size of the input through a special convolution process to rebuild the input data in the output, making sure it is the same size as it was originally.

Figure 7a–d provide examples of this reconstruction process using induced shaft voltage measurements in both time-domain and frequency-domain representations. Notably, as illustrated in Fig. 7b and d, the CAE model struggles to reconstruct instances of faulty data accurately. This discrepancy results in a noticeable error between the original and reconstructed data, highlighting this approach's capability to identify anomalies.

3.2 Threshold determination

For anomaly detection using the reconstruction error obtained by the CAE model, there should be a fault threshold to differentiate between healthy and faulty (anomaly) cases. In this study, the fault threshold is established based on the maximum reconstruction error observed in the training dataset. Existing works on data-driven anomaly detection across various applications have established similar fault thresholds based on the reconstruction error for healthy training data (Chen et al., 2021; Xiang et al., 2022; Campoverde-Vilela et al., 2023; Givnan et al., 2022). The training data comprise instances representing the healthy state of the PMSG. As mentioned, each training sample $x^{(i)}$ is passed through the CAE model to obtain a reconstructed output $\hat{x}^{(i)}$. The discrepancy between the original and reconstructed data points, quantified using the MSE cost function, serves as the reconstruction error $e^{(i)} = \mathrm{MSE}(x^{(i)}, \hat{x}^{(i)})$. The fault threshold α is then determined as the maximum reconstruction error observed in the training data as follows:

$$\alpha = \max_{i=1}^{N} e^{(i)}, \tag{4}$$

where N is the size of the training dataset. As an example, Fig. 8a and b show the histogram of reconstruction errors or anomaly scores for training (healthy) data and the fault threshold determination for two distinct measurements. These figures clearly demonstrate that the thresholds are data-driven, varying in accordance with the input measurements of the CAE model. Any test sample with a reconstruction error exceeding the threshold would be considered an anomaly.
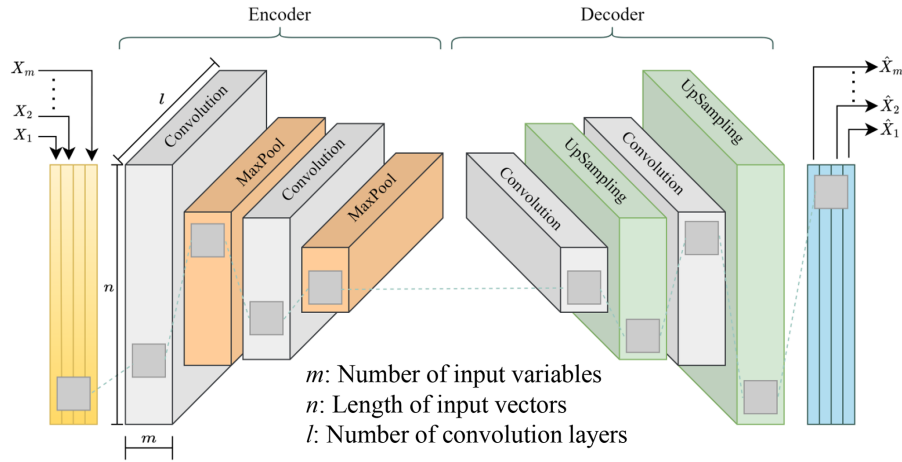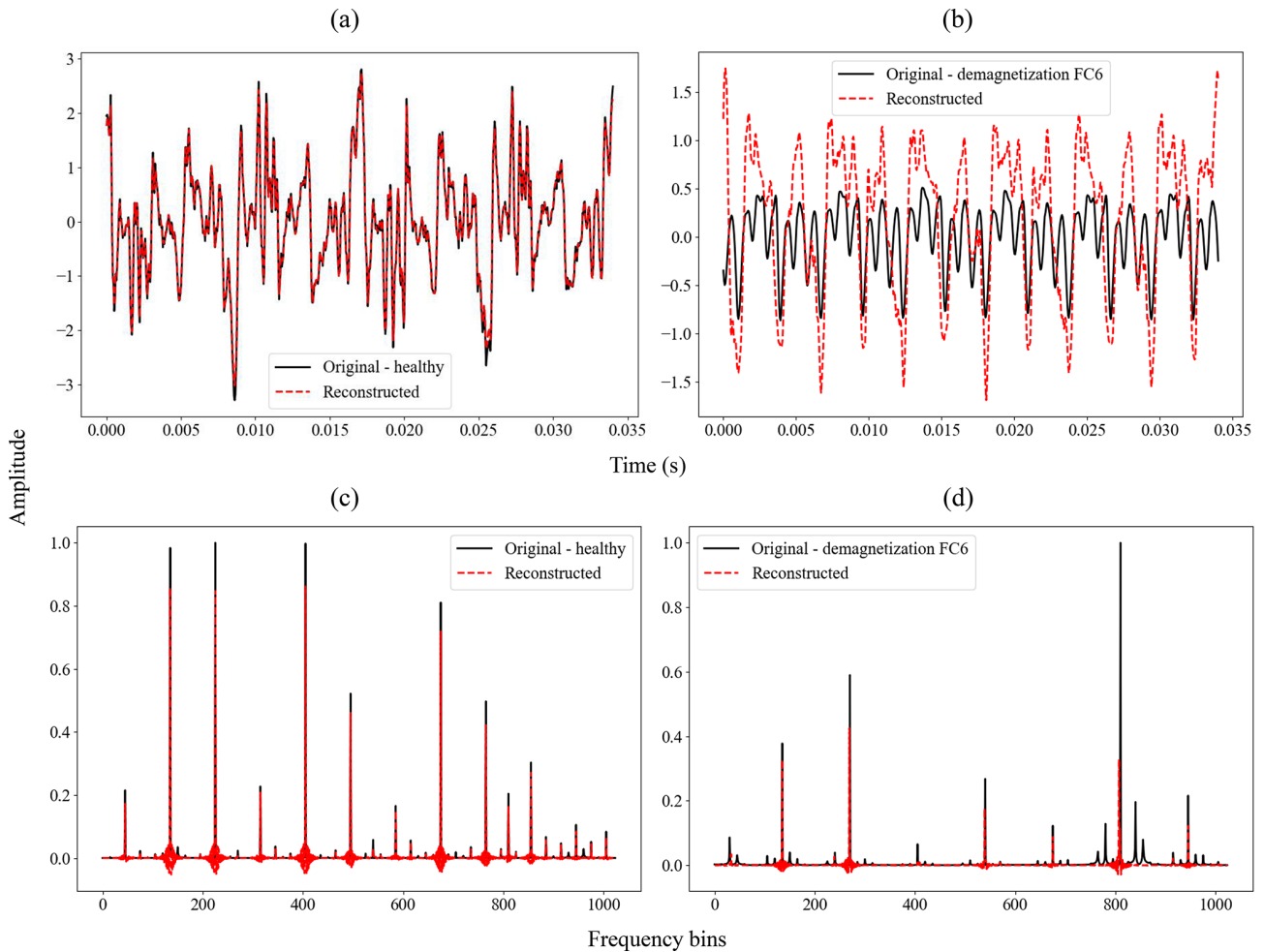
Figure 6. Convolutional autoencoder architecture.

Figure 7. Comparison between the original input and reconstructed output of the CAE model for the induced shaft voltage signal: **(a)** time domain – healthy, **(b)** time domain – demagnetization FC6, **(c)** frequency domain – healthy, and **(d)** frequency domain – demagnetization FC6.
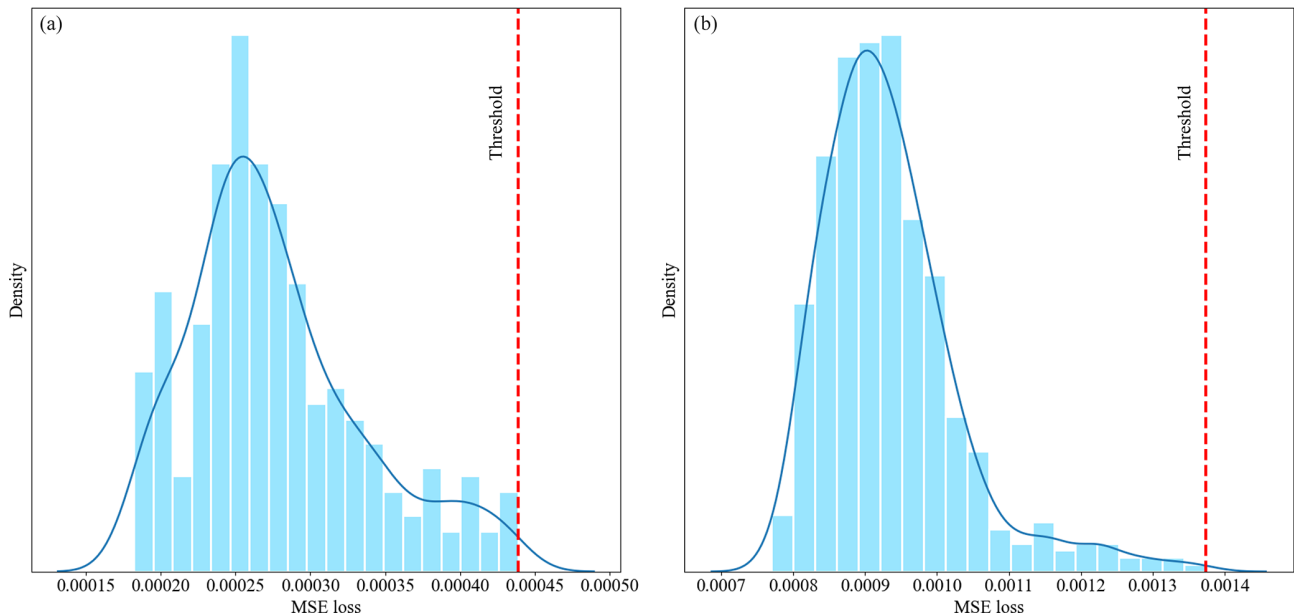
Figure 8. Histogram of anomaly scores for training data and threshold determination for two different signals: **(a)** SFt5 and **(b)** AFtt.

3.3 Overall procedure of the anomaly detection method

The steps taken in the anomaly detection of the PMSG model are briefly described in this section and outlined in Fig. 9. The methodology includes several stages as follows.

1. *Data collection*. The initial step involves the comprehensive gathering of target measurements, introduced in Table 2, from the PMSG model.

2. *Data preprocessing*. Once collected, the measurements are preprocessed. As the first step, the signals are segmented into shorter-length signals to prepare training, validation, and test datasets for the CAE model. Segmented signals are then normalized to aid in efficient training, prevent numerical issues, and ultimately lead to better model performance and generalization. Both time-domain and frequency-domain measurements are fed into the model to compare the model performance in both cases for different measurements.

3. *Model training*. With the data prepared, the next phase is the training of the CAE model. It should be noted that distinct CAE models are trained for different measurements, depending on the type of input data, either the time domain or frequency domain. The model learns to identify patterns and features of the input data representative of the normal operational state of the PMSG model.

4. *Threshold determination*. As discussed in Sect. 3.2, a key aspect of the methodology is establishing a reliable fault threshold. The optimal choice of this threshold is crucial for effectively differentiating between normal
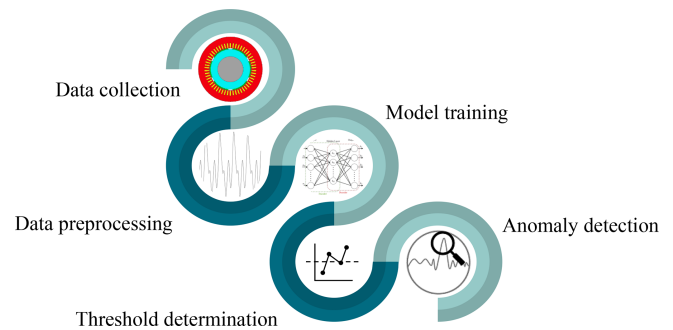

Figure 9. Overall procedure of the anomaly detection method.

and faulty states and ensuring a precise alarm triggering. This study utilizes the maximum reconstruction error value from the training dataset as the fault threshold.

5. *Anomaly detection*. The final step involves the actual detection of anomalies. The trained CAE model is employed to analyze new data, identifying deviations from the norm. Any reconstruction error exceeding the established fault threshold is considered indicative of an anomaly in the PMSG model.

3.4 Performance metrics

In this study, two performance metrics are used to evaluate the performance of the CAE model for anomaly detection.

– *F1 score*. This metric combines precision and recall to provide a single score for the model's overall accuracy in anomaly detection (Miele et al., 2022; Wang et al.,

2019). Precision indicates what proportion of identified anomalies are true anomalies, and its equation is as follows:

$$\text{precision} = \frac{\text{TP}}{\text{TP} + \text{FP}}, \tag{5}$$

where TP is the number of correctly identified anomalies (true positive) and FP is the number of normal samples misclassified as anomalies (false positive). Recall also specifies what proportion of true anomalies are identified and is determined as follows:

$$\text{recall} = \frac{\text{TP}}{\text{TP} + \text{FN}}, \tag{6}$$

where FN is the number of anomaly samples misclassified as normal (false negative). The F1 score ranges from 0 to 1, where 1 represents perfect precision and recall, and is defined as follows:

$$\text{F1 score} = 2 \times \frac{\text{precision} \times \text{recall}}{\text{precision} + \text{recall}}. \tag{7}$$

– *Silhouette coefficient*. This metric assesses the quality of clustering in unsupervised machine learning tasks, with scores ranging from -1 to 1 (Rousseeuw, 1987). In this study, the silhouette score is used to calculate the average distance between the cluster of identified anomalies and the cluster of healthy data. A higher silhouette coefficient indicates better separation between normal and anomaly clusters. The silhouette coefficient for each sample i is calculated as follows:

$$\text{SC}^{(i)} = \frac{b^{(i)} - a^{(i)}}{\max[a^{(i)}, b^{(i)}]}, \tag{8}$$

where $a^{(i)}$ is the average distance between sample i and all other samples in the same cluster and $b^{(i)}$ is the minimum distance between sample i and all samples in another cluster not containing sample i.

Both metrics provide comprehensive insights into the performance and reliability of the CAE model in detecting anomalies using different measurement variables.

4 Results and discussion

4.1 Data preparation

The procedure for anomaly detection begins with collecting simulated measurements from the PMSG model under both healthy and various faulty conditions. These measurements are then divided into shorter-length signals to ensure an adequate amount of training and test data for the CAE model. To compare the performance of different measurements, both time-domain data (raw segmented signals) and frequency-domain data (spectrum of segmented signals) are

inputted into the CAE model. Following the standard approach for anomaly detection, the training dataset consists only of measurements from the healthy state, while the test dataset encompasses all states, including healthy and different faulty conditions. The original signals are sampled at a rate of $F_s = 21.132 \, \text{kHz}$. The fundamental frequency of the generator model under study is calculated as $f = (N_s \times P)/120 = 58.69 \, \text{Hz}$, where N_s represents the synchronous speed of the generator at its rated speed of 1173.7 rpm and P denotes the number of poles (six in this case).

For time-domain data inputted into the CAE model, the length of segmented signals is set to twice the period of the fundamental frequency, resulting in 720 sample points per segment. Additionally, the segmentation process includes overlap between consecutive segments equivalent to one period of the fundamental frequency, which is 360 sample points. It is important to highlight that for frequency-domain data, where a higher resolution in obtaining the frequency spectrum is required, the segmented signals have a longer duration of 30 times the period of the fundamental frequency or 10 800 sample points. This longer duration leads to smaller training and test datasets for the frequency-domain cases compared to the time-domain cases. It should be noted that only the first 720 sample points of the frequency spectrum are fed into the model in order to have the same CAE model architecture for time-domain and frequency-domain cases. The segmentation and feeding procedure into the CAE model for both time-domain and frequency-domain cases is illustrated in Fig. 10.

4.2 Anomaly detection results: time-domain inputs

The CAE model's reconstruction errors or anomaly scores trained with time-domain data for demagnetization and eccentricity faults are illustrated in Figs. 11 and 12, respectively. These figures highlight the reconstruction error values within a yellow region for the set of healthy training samples, where the highest error value defines the fault threshold, marked by a horizontal dotted red line. Similarly, the green region represents the reconstruction errors for healthy test samples. The outcomes of performance metrics are detailed in Table 5. According to the F1 score results, nearly all signals can train a CAE model that effectively detects demagnetization fault cases. In contrast, for eccentricity fault cases, only specific signals – induced shaft voltage (Vsh), electromagnetic torque (Te), stator phase currents (Is), and the tangential component of air gap flux at tooth positions (AFtt) – achieve full accuracy in fault detection. The silhouette coefficient, which measures the degree of separation between anomaly clusters and the healthy cluster, shows that Vsh, Te, Is, and AFtt signals provide superior separation for both demagnetization and eccentricity faults.

The sensitivity of the CAE model to fault severity is also evaluated using the trend of anomaly score values for fault scenarios. It is expected that cases with higher fault sever-
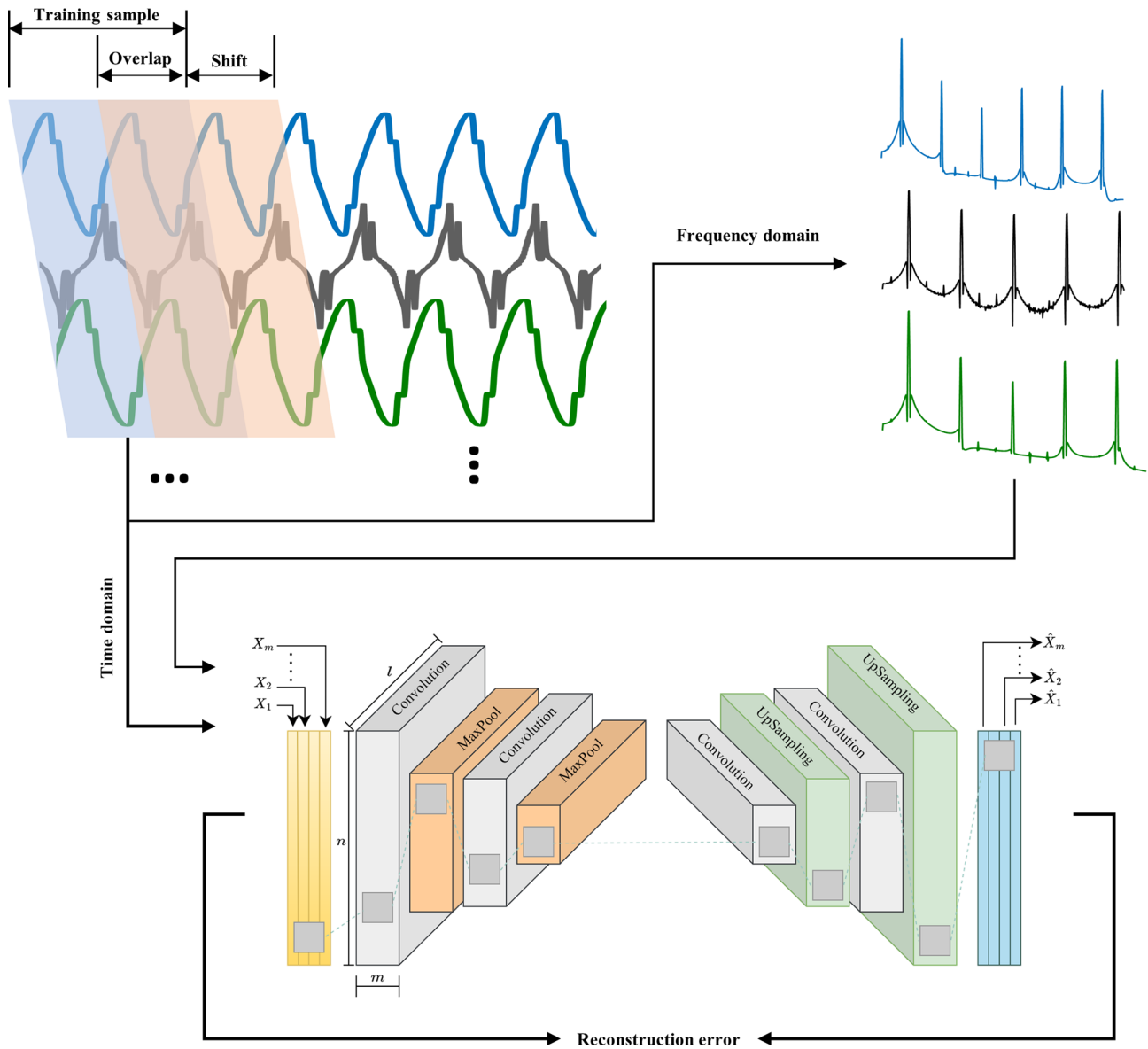
Figure 10. Signal segmentation process.

ity should correspond to higher anomaly scores. Among the models trained with the signals featured, the model trained with three-phase Is signals demonstrates sensitivity to the severity across all types of demagnetization faults, as illustrated in Fig. 11d. However, the Vsh-based trained model does not adequately reflect the severity for FC3 and FC4 cases, which are localized demagnetization in one pole, with the anomaly scores for FC4 unexpectedly lower. Other models, including those trained with Te, stray, and air gap flux signals, fail to differentiate between the severities of FC5 and FC6 cases, both involving localized demagnetization across all poles.

For eccentricity faults, both dynamic (FC1–FC3) and static (FC4–FC6), as presented in Fig. 12, the Is and Vsh sig-nals are effective in distinguishing between different degrees of eccentricity for both cases, with anomaly scores increasing as the degree of eccentricity raises. However, outputs of the CAE model trained with the Te signal do not display a consistent trend with respect to the eccentricity degree. The results for FC2 test samples, which exhibit a 15 % dynamic eccentricity, are also poor when the model is trained with AFtt signals.

In summary, the CAE model, trained with time-domain data from three-phase stator currents, reliably provides anomaly detection for both demagnetization and eccentric-ity fault cases. The efficacy of this model with frequency-domain data will be further assessed in subsequent analyses.
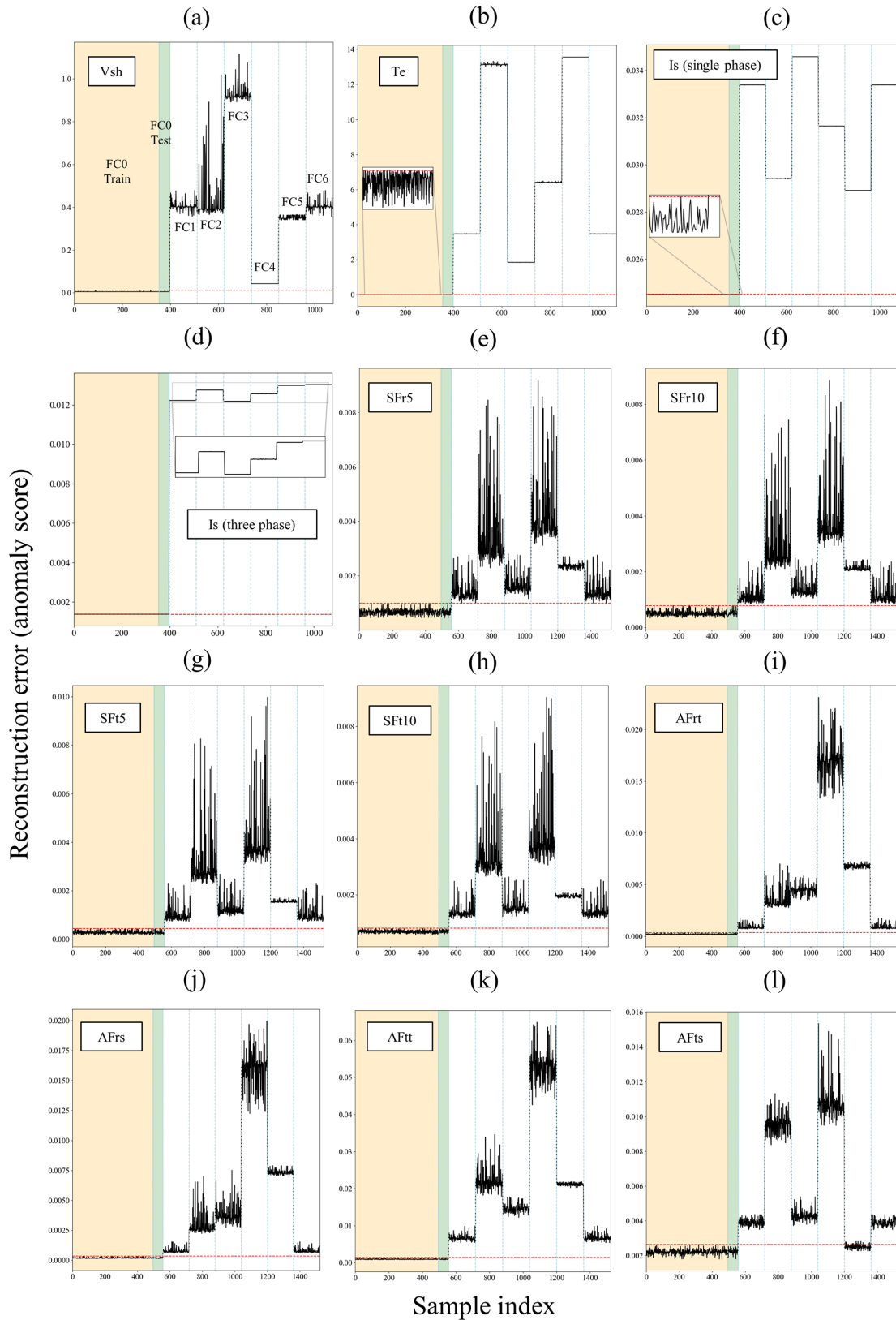
Figure 11. Anomaly detection results of time-domain measurements for demagnetization fault cases: **(a)** Vsh, **(b)** Te, **(c)** Is (single phase), **(d)** Is (three phases), **(e)** SFr5, **(f)** SFr10, **(g)** SFt5, **(h)** SFt10, **(i)** AFrt, **(j)** AFrs, **(k)** AFtt, and **(l)** AFts.
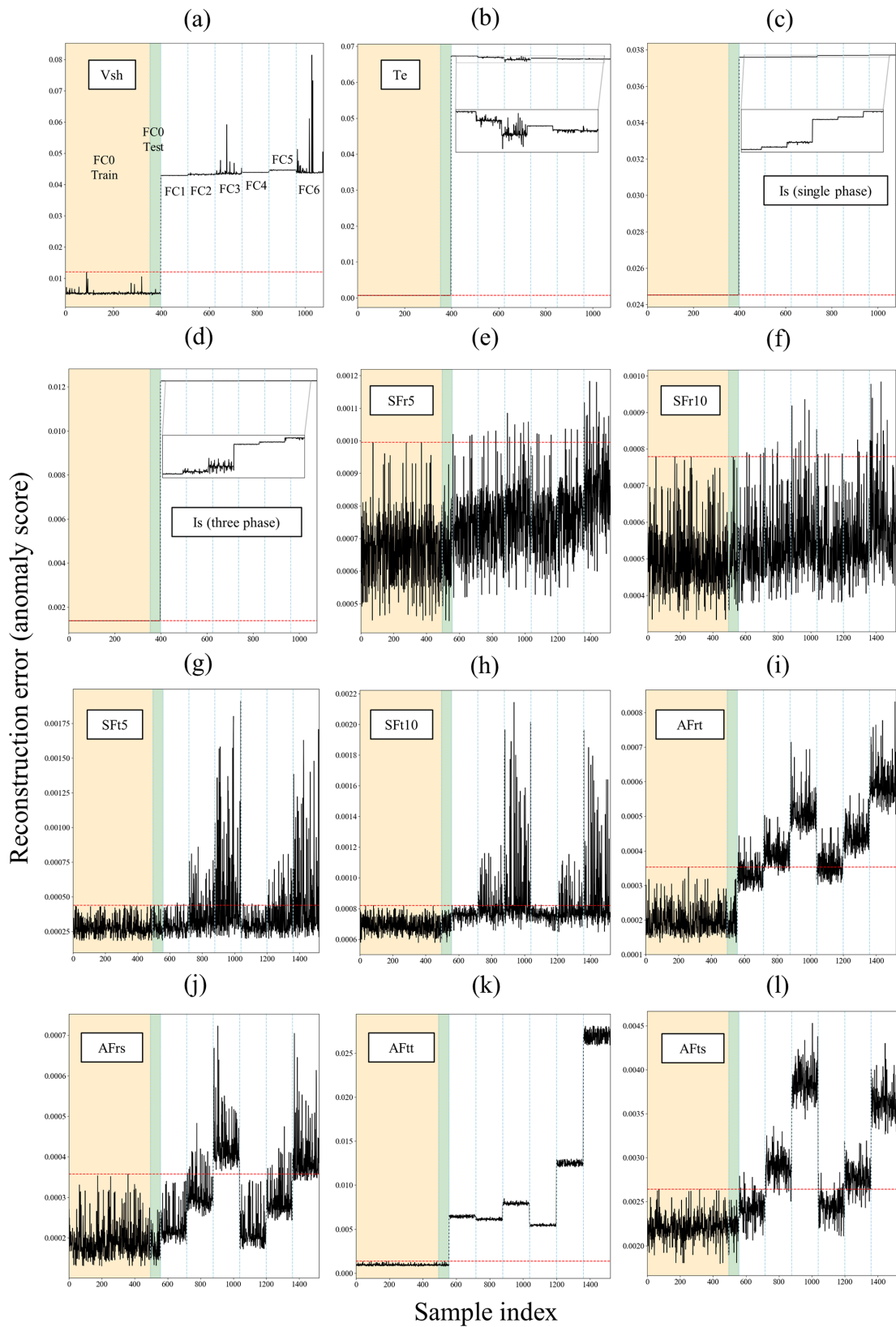
Figure 12. Anomaly detection results of time-domain measurements for static and dynamic eccentricity fault cases: **(a)** Vsh, **(b)** Te, **(c)** Is (single phase), **(d)** Is (three phases), **(e)** SFr5, **(f)** SFr10, **(g)** SFt5, **(h)** SFt10, **(i)** AFrt, **(j)** AFrs, **(k)** AFtt, and **(l)** AFts.

Table 5. Performance metric results of anomaly detection models trained with time-domain data.

Input variable	Demagnetization		Eccentricity	
	F1	Silhouette	F1	Silhouette
Vsh	1.0000	0.9863	1.0000	0.9890
Te	1.0000	0.9996	1.0000	0.9998
Is (single phase)	0.9993	0.9999	0.9993	0.9998
Is (three phases)	1.0000	0.9999	1.0000	0.9999
SFr5	0.9980	0.8592	0.0650	0.1690
SFr10	1.0000	0.8600	0.0690	0.0840
SFt5	1.0000	0.8990	0.3000	0.2400
SFt10	1.0000	0.9100	0.3400	0.3500
AFrt	1.0000	0.9500	0.8700	0.7800
AFrs	1.0000	0.9400	0.5100	0.4900
AFtt	1.0000	0.9721	1.0000	0.9835
AFts	0.9300	0.8600	0.8000	0.6600

Table 6. Performance metric results of anomaly detection models trained with frequency-domain data.

Input variable	Demagnetization		Eccentricity	
	F1	Silhouette	F1	Silhouette
Vsh	1.00	0.9912	0.9733	0.9321
Te	1.00	0.9999	1.0000	0.9922
Is (single phase)	–	–	0.8623	0.7760
Is (three phases)	–	–	0.8230	0.6561
SFr5	1.00	0.9220	0.9692	0.7914
SFr10	1.00	0.9190	0.7300	0.8580
SFt5	1.00	0.9320	1.0000	0.6943
SFt10	1.00	0.9500	1.0000	0.700
AFrt	0.91	0.9620	1.0000	0.9400
AFrs	0.91	0.9670	0.6900	0.9400
AFtt	0.91	0.9845	1.0000	0.9899
AFts	0.91	0.9950	0.7000	0.9400

4.3 Anomaly detection results: frequency-domain inputs

In this section, segmented signals are transformed into the frequency domain. This transformation allows for the frequency information of simulated data to be utilized by the CAE model, thereby enhancing its predictive accuracy. The use of frequency-domain information has been found to improve prediction outcomes for certain signals. To illustrate this, the power spectral density (PSD) spectra for a variety of signals are shown in Fig. 13. These include healthy data, demagnetization in FC5 and FC6 (two segments of all poles), and static eccentricity (FC4–FC6). Upon examination of these figures, it is observed that fluctuations in the frequency content associated with faults, as well as the appearance of characteristic fault frequencies, are more prominently visible in specific signals, notably those from flux sensors and electromagnetic torque.

Similar to the anomaly detection results in the time domain, the anomaly scores for frequency-domain training and test samples, utilizing various models, are depicted in Figs. 14 and 15 for demagnetization and eccentricity faults, respectively. Additionally, the performance of these models is evaluated and presented in terms of F1 and silhouette scores, as shown in Table 6.

The CAE model, when trained with the Vsh signal, demonstrates reliable anomaly detection results in demagnetization cases, as depicted in Fig. 14a, highlighting both the detection accuracy and sensitivity to fault severity. However, in the context of eccentricity faults, this model exhibits somewhat poorer performance in detecting FC3 (25 % dynamic eccentricity) and in being sensitive to different levels of fault severity, as illustrated in Fig. 15a.

While the Te signal achieves full detection accuracy for both types of faults according to Table 6, similar to the results in the time domain, the anomaly scores do not align with the actual severity levels of the fault cases. This discrepancy is evident in the results depicted in Figs. 14b and 15b.

Stator current signals (Is) yield anomaly scores that are entirely below the fault threshold line for demagnetization cases and partially below it for eccentricity cases, as illustrated in Figs. 14 and 15c and d. This outcome aligns with expectations, as the comparison of the frequency spectra of the Is signal between healthy and faulty states, shown in Fig. 13e and f, reveals only minor shifts attributable to the faults. Furthermore, it is noteworthy that, according to Figs. 14 and 15c and d, the CAE model tends to assign lower anomaly scores to faulty samples than to healthy ones. This issue is attributed to the subtle feature shifts caused by faults and the CAE model's complexity, which enables it to capture a broad spectrum of features, including those not directly indicative of anomalies. The model's high complexity, advantageous for identifying complex patterns in normal data, might also unexpectedly improve its ability to reconstruct faulty samples. This is because the model, with its extensive layers and multitude of parameters, can generalize well to data variations that resemble the healthy samples it was trained on, even if they are not identical. Consequently, subtle feature shifts due to faults are not adequately penalized, resulting in lower anomaly scores for faulty samples. This phenomenon is not unique to stator current signals; it has also been observed in other scenarios, such as the FC5 demagnetization case with air gap flux sensors, as depicted in Fig. 14i–l. Addressing this issue requires a comprehensive understanding of model complexity and its effects on anomaly detection, which is beyond the scope of this study.

Stray flux sensors, both radial and tangential components, demonstrate strong performance by achieving full accuracy and sensitivity in demagnetization cases, as evidenced in Fig. 14e–k. In the context of eccentricity faults, the radial components (SFr5 and SFr10) exhibit effective detection of dynamic eccentricity (FC1–FC3) test samples, with the severity levels being distinctly identifiable. However, these
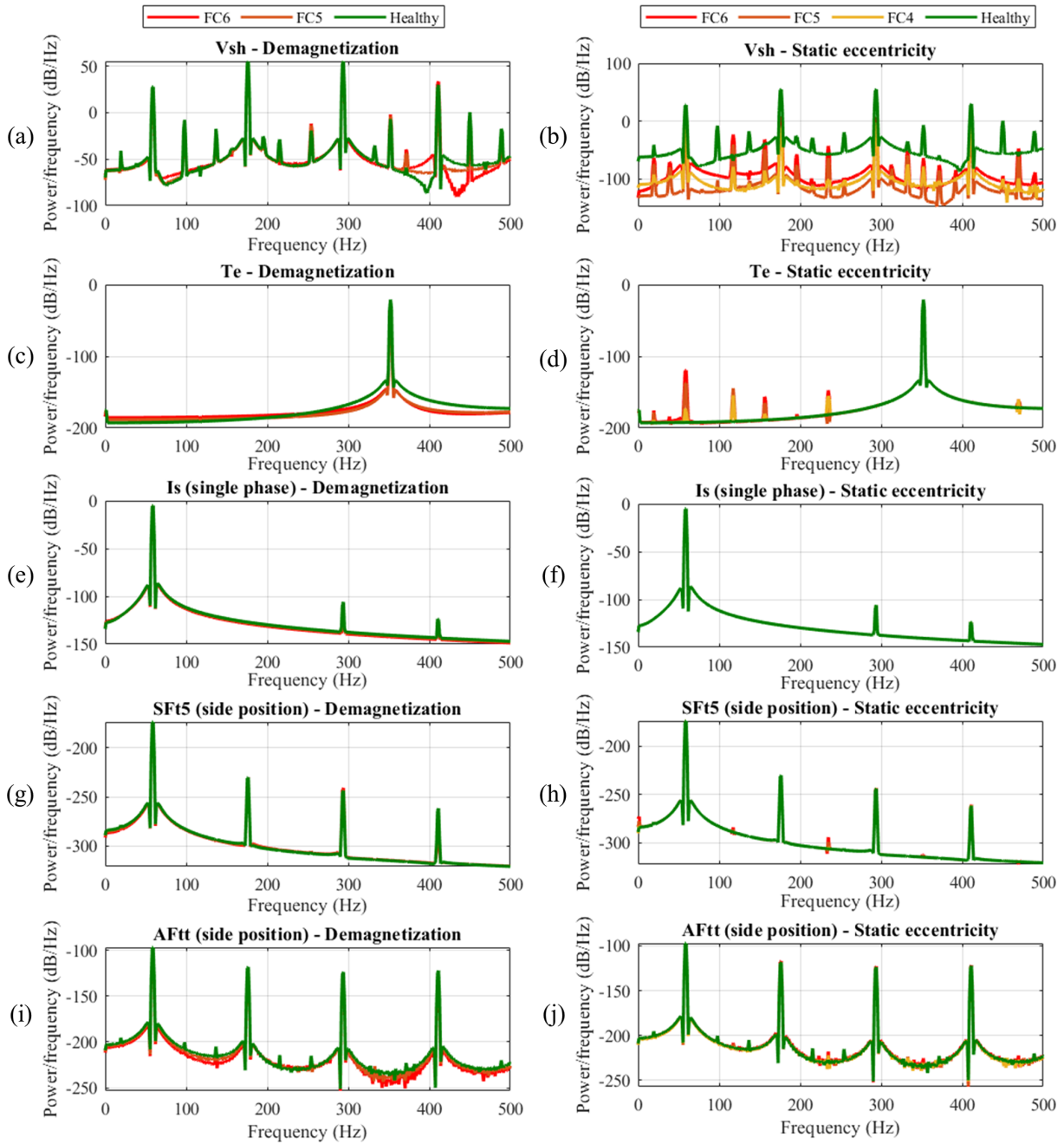
Figure 13. Power spectral density plots of simulated signals under healthy and faulty states.

signals, particularly SFr10, fail to detect some test samples associated with static eccentricity (FC4–FC6), as reflected by the F1 scores (96.92 % for SFr5 and 73 % for SFr10) in Table 6 and Fig. 15e and f. On the other hand, tangential component signals (SFt5 and SFt10) achieve full F1 scores, and the models trained on these signals are sensitive to varying severity levels of both dynamic and static eccentricities, as shown in Fig. 15g and h. Nevertheless, based on silhouette scores, it is observed that radial components offer a superior

separation between healthy and faulty clusters in cases of eccentricity faults.

Regarding air gap flux sensors, the anomaly scores related to demagnetization, as presented in Fig. 14i–l, reveal an inability to detect test samples for FC5, which represents a low-severity, localized demagnetization affecting all poles. Furthermore, both the radial and tangential components of the air gap flux sensors positioned at the slot (AFrs and AFts) fail to detect static eccentricity cases, as indicated in Fig. 15j and l. However, the tooth sensor, especially its tangential compo-
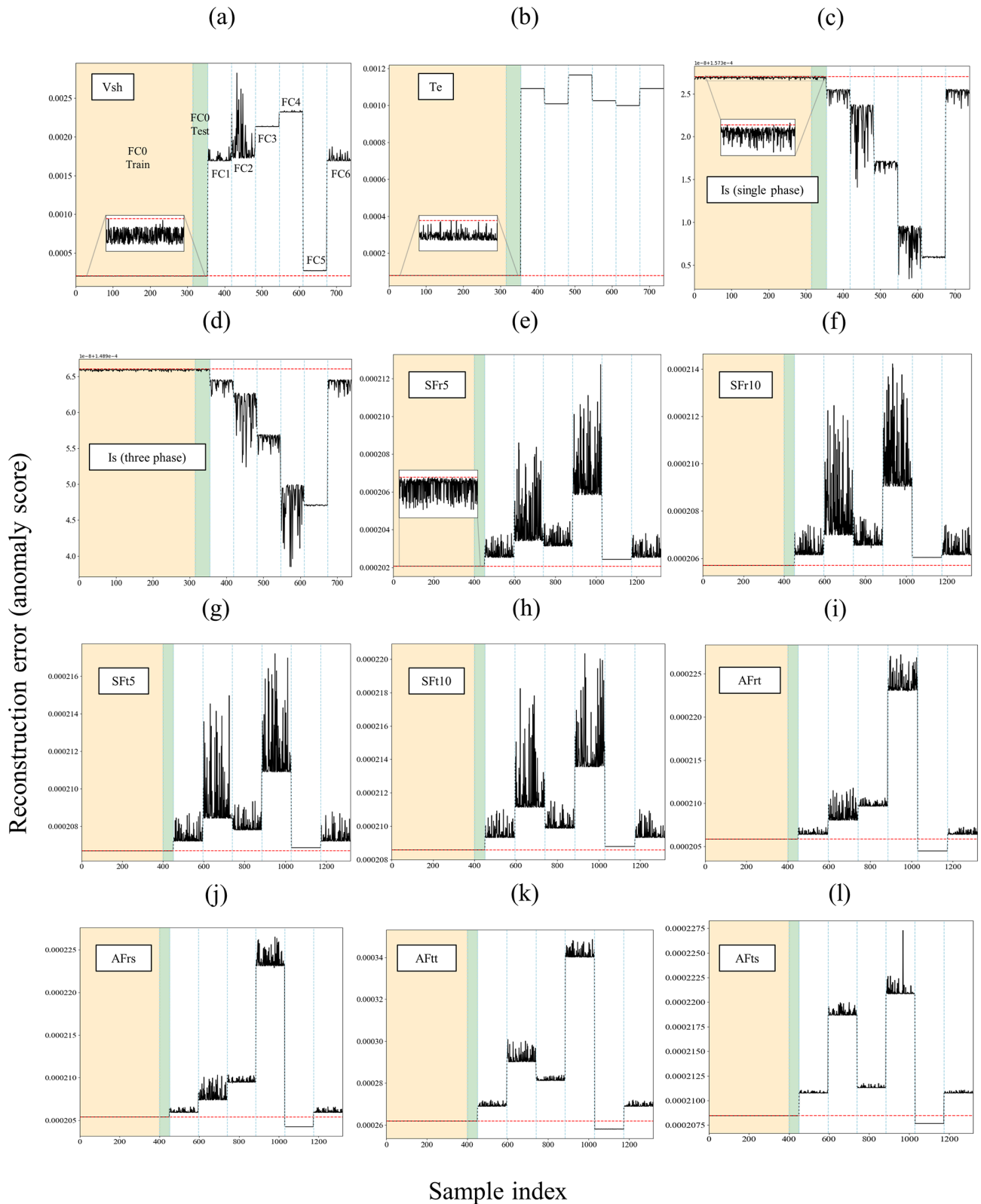
Figure 14. Anomaly detection results of frequency-domain measurements for demagnetization fault cases: **(a)** Vsh, **(b)** Te, **(c)** Is (single phase), **(d)** Is (three phases), **(e)** SFr5, **(f)** SFr10, **(g)** SFt5, **(h)** SFt10, **(i)** AFrt, **(j)** AFrs, **(k)** AFtt, and **(l)** AFts.
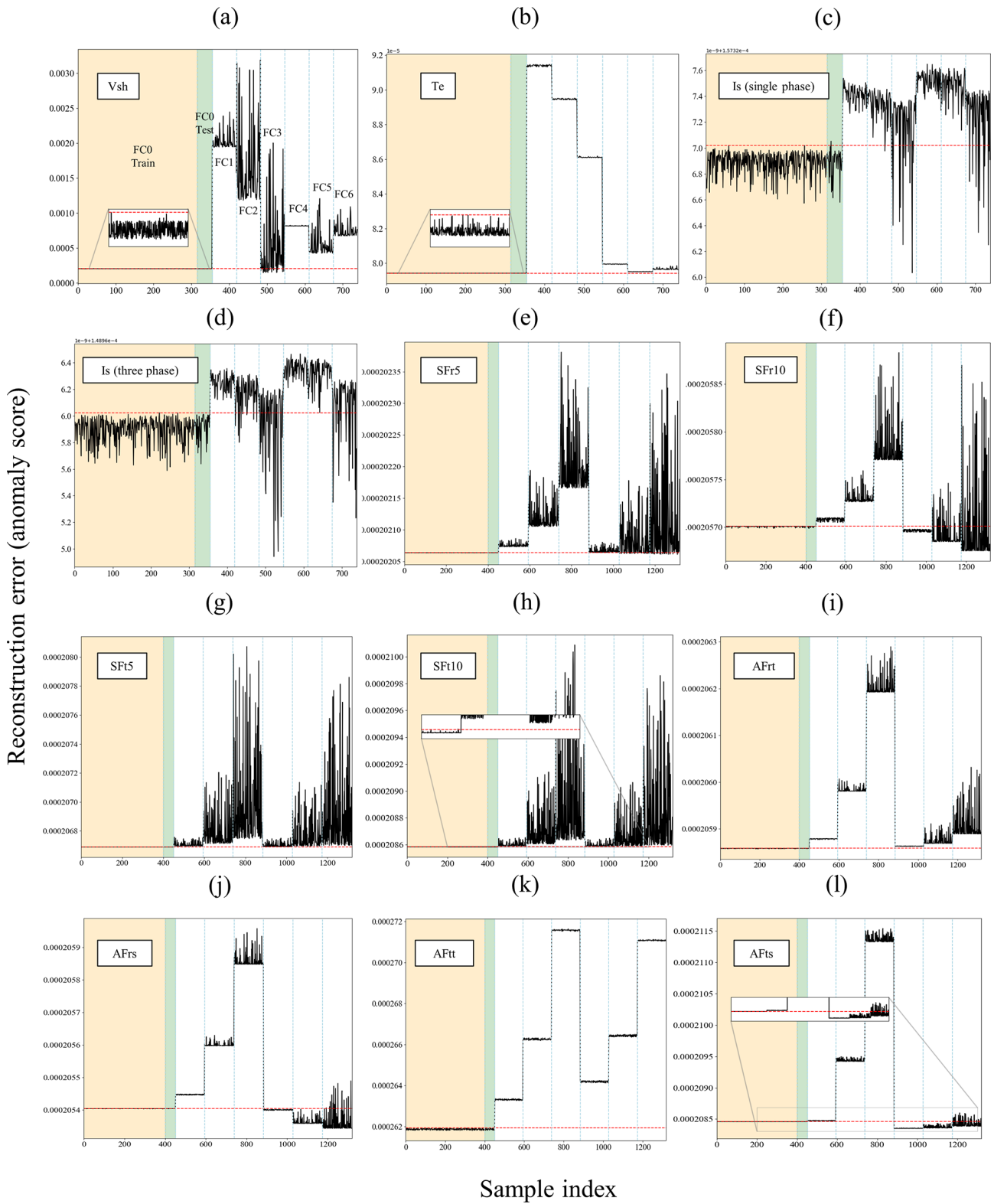
Figure 15. Anomaly detection results of frequency-domain measurements for static and dynamic eccentricity fault cases: **(a)** Vsh, **(b)** Te, **(c)** Is (single phase), **(d)** Is (three phases), **(e)** SFr5, **(f)** SFr10, **(g)** SFt5, **(h)** SFt10, **(i)** AFrt, **(j)** AFrs, **(k)** AFtt, and **(l)** AFts.

nent (AFtt), gives precise results for eccentricity cases that accurately reflect the severity levels of the faults, as demonstrated in Fig. 15k.

In summary, CAE models trained on the frequency content from stray flux sensors at all four top, bottom, and side positions – tangential components at both 5 mm and 10 mm distance and radial components at 5 mm distance outside the stator housing – demonstrate full accuracy and sensitivity in detecting anomalies associated with both demagnetization and eccentricity faults. Moreover, the radial and tangential components of air gap flux sensors located at the tooth are fully capable of identifying all types of eccentricity anomalies, accurately reflecting their severity levels. These findings highlight the potential of adopting flux monitoring techniques – well-established in other industries for their cost-efficient and easy-to-install sensors – in the fault detection of large MW offshore wind generators. The utilization of such sensors, especially stray flux sensors enhanced with frequency information, presents a promising strategy for the condition monitoring of these systems.

To conclude the discussion section, Table 7 provides a comprehensive and detailed summary of all anomaly detection outcomes derived from the previously analyzed signals. This table outlines the detection accuracy for each fault case, alongside the sensitivity to fault severity, across both time and frequency domains. The table is organized such that the first row associated with each domain presents the detection accuracy results, while the second row specifies whether the signal in question is capable of monitoring changes in fault severity levels. It should be noted that for the purposes of this table, detection accuracies exceeding 95 % are considered to constitute acceptable accuracy. This structured presentation ensures a clear and concise overview of the study's findings.

4.4 Fault discrimination capability of selected measurements

This section evaluates the performance of the CAE anomaly detection model, focusing on its fault discrimination capability. The analysis covers models trained on selected signals from both the time and frequency domains, as discussed in earlier sections and presented in Table 7. The CAE model, trained with time-domain signals of three-phase current Is, achieved perfect accuracy in detecting anomalies and showed sensitivity to variations in fault severities, as depicted in Figs. 11d and 12d. In the frequency domain, models trained with stray flux signals – tangential components both at 5 mm (SFt5) and 10 mm (SFt10) distance and radial components at 5 mm distance (SFr5) – proved to be more effective in detecting anomalies than others.

The ability of these models to distinguish between two specific types of faults is assessed by analyzing the reconstruction errors. This analysis is presented in Fig. 16a–d for Is, SFt5, SFt10, and SFr5 signals, respectively. While Is signals allow for perfect differentiation between different fault

cases, there is a noticeable overlap in anomaly score ranges between eccentricity and demagnetization faults, as shown in Fig. 16a. This overlap makes establishing a clear separation boundary challenging between eccentricity and demagnetization, as anomaly scores for FC1 and FC3 demagnetization faults are lower than those for eccentricity faults. A similar issue is observed with the tangential stray flux (SFt5 and SFt10) measurements, as indicated in Fig. 16b and c. However, the CAE model trained with radial stray flux (SFr5) measurements demonstrates a clear ability to differentiate between the two fault types based on their anomaly scores, as shown in Fig. 16c.

These findings indicate that radial stray flux measurements, taken from 5 mm outside the stator housing, not only accurately detect anomalies and assess fault severity but also effectively distinguish between eccentricity and demagnetization faults in PMSG. Further exploration of fault classification and diagnosis will be the focus of future work.

4.5 Comparison with other machine learning models

As a comparison study and to prove the robustness of the CAE anomaly detection model, this section includes a comparison of three distinct models for unsupervised anomaly detection: one-class support vector machine (SVM), k-nearest neighbor (KNN) model, and k-means model. All models are trained on a dataset of 400 normal samples using time-domain data of three-phase current measurements (Is) and tested using 100 untrained normal samples and 100 samples under demagnetization and eccentricity fault conditions. The one-class SVM, employing a radial basis function (RBF) kernel, focuses on defining a decision function that envelops the region of normal data, treating all other areas as anomalies. The k-means model, configured with a single cluster, detects anomalies based on the distance from data points to the centroid of normal data, with a threshold set at the 99th percentile of these distances. The KNN model, using 10 neighbors, identifies anomalies based on the average distance to the nearest neighbors, applying a threshold at the 99th percentile to define outliers. Each model's performance was evaluated based on its F1 score and accuracy, with results summarized in Table 8 and illustrated through confusion matrices in Fig. 17. The CAE model achieved the highest accuracy at 100 %, while the compared traditional models recorded accuracies between 85 %–90 %. It should be noted that the performance of these traditional models may diminish as data complexity increases, highlighting challenges in scaling these models to more complex or larger datasets. On the other hand, it should also be noted that the CAE deep learning model requires extensive fine tuning of numerous hyperparameters and significantly longer training times.

Table 7. Summary of anomaly detection results.

Signal	Domain	Studied fault											
		Demagnetization						Eccentricity					
		FC1	FC2	FC3	FC4	FC5	FC6	FC1	FC2	FC3	FC4	FC5	FC6
Vsh	Time	✓	✓	✓	✓	✓	✓	✓	✓	✓	✓	✓	✓
		✓		x		✓		✓			✓		
	Freq.	✓	✓	✓	✓	✓	✓	✓	✓	✓	✓	✓	✓
		✓		✓		✓		x			x		
Te	Time	✓	✓	✓	✓	✓	✓	✓	✓	✓	✓	✓	✓
		✓		✓		x		x			x		
	Freq.	✓	✓	✓	✓	✓	✓	✓	✓	✓	✓	✓	✓
		x		x		✓		x			x		
Is – one phase	Time	✓	✓	✓	✓	✓	✓	✓	✓	✓	✓	✓	✓
		x		x		✓		✓			✓		
	Freq.	x	x	x	x	x	x	✓	✓	x	✓	✓	x
		x		x		x		x			x		
Is – three phases	Time	✓	✓	✓	✓	✓	✓	✓	✓	✓	✓	✓	✓
		✓		✓		✓		✓			✓		
	Freq.	x	x	x	x	x	x	✓	x	x	✓	✓	x
		x		x		x		x			x		
SFr5	Time	✓	✓	✓	✓	✓	✓	x	x	x	x	x	x
		✓		✓		x		x			x		
	Freq.	✓	✓	✓	✓	✓	✓	✓	✓	✓	✓	✓	✓
		✓		✓		✓		✓			✓		
SFt5	Time	✓	✓	✓	✓	✓	✓	x	x	x	x	x	x
		✓		✓		x		x			x		
	Freq.	✓	✓	✓	✓	✓	✓	✓	✓	✓	✓	✓	✓
		✓		✓		✓		✓			✓		
SFr10	Time	✓	✓	✓	✓	✓	✓	x	x	x	x	x	x
		✓		✓		x		x			x		
	Freq.	✓	✓	✓	✓	✓	✓	✓	✓	✓	x	x	x
		✓		✓		✓		✓			x		
SFt10	Time	✓	✓	✓	✓	✓	✓	x	x	x	x	x	x
		✓		✓		x		x			x		
	Freq.	✓	✓	✓	✓	✓	✓	✓	✓	✓	✓	✓	✓
		✓		✓		✓		✓			✓		
AFrt	Time	✓	✓	✓	✓	✓	✓	x	✓	✓	x	✓	✓
		✓		✓		x		✓			✓		
	Freq.	✓	✓	✓	✓	x	✓	✓	✓	✓	✓	✓	✓
		✓		✓		✓		✓			✓		
AFtt	Time	✓	✓	✓	✓	✓	✓	✓	✓	✓	✓	✓	✓
		✓		✓		x		x			✓		
	Freq.	✓	✓	✓	✓	x	✓	✓	✓	✓	✓	✓	✓
		✓		✓		✓		✓			✓		
AFrs	Time	✓	✓	✓	✓	✓	✓	x	x	✓	x	x	✓
		✓		✓		x		✓			✓		
	Freq.	✓	✓	✓	✓	x	✓	✓	✓	✓	x	x	x
		✓		✓		✓		✓			x		
AFts	Time	✓	✓	✓	✓	x	✓	x	✓	✓	x	✓	✓
		✓		✓		✓		✓			✓		
	Freq.	✓	✓	✓	✓	x	✓	✓	✓	✓	x	x	x
		✓		✓		✓		✓			x		

Abbreviations: Vsh, induced shaft voltage; Te, electromagnetic torque; Is, stator phase current; SFr5, stray flux sensor – radial component, outside stator housing with a distance of 5 mm (four signals); SFt5, stray flux sensor – tangential component, outside stator housing with a distance of 5 mm (four signals); SFr10, stray flux sensor – radial component, outside stator housing with a distance of 10 mm (four signals); SFt10, stray flux sensor – tangential component, outside stator housing with a distance of 10 mm (four signals); AFrt, air gap flux sensor – radial component at tooth position (four signals); AFtt, air gap flux sensor – tangential component at tooth position (four signals); AFrs, air gap flux sensor – radial component at slot position (four signals); AFts, air gap flux sensor – tangential component at slot position (four signals). Demagnetization: FC1, all segments of one pole (10 %); FC2, all segments of one pole (20 %); FC3, two segments of one pole (40 % and 20 %); FC4, two segments of one pole (80 % and 40 %); FC5, two segments of all poles (20 % and 10 %); FC6, two segments of all poles (40 % and 20 %). Eccentricity: FC1–FC3, dynamic (5 %–25 %); FC4–FC6, static (5 %–25 %). ✓: fault condition detectable; x: fault condition not detectable.
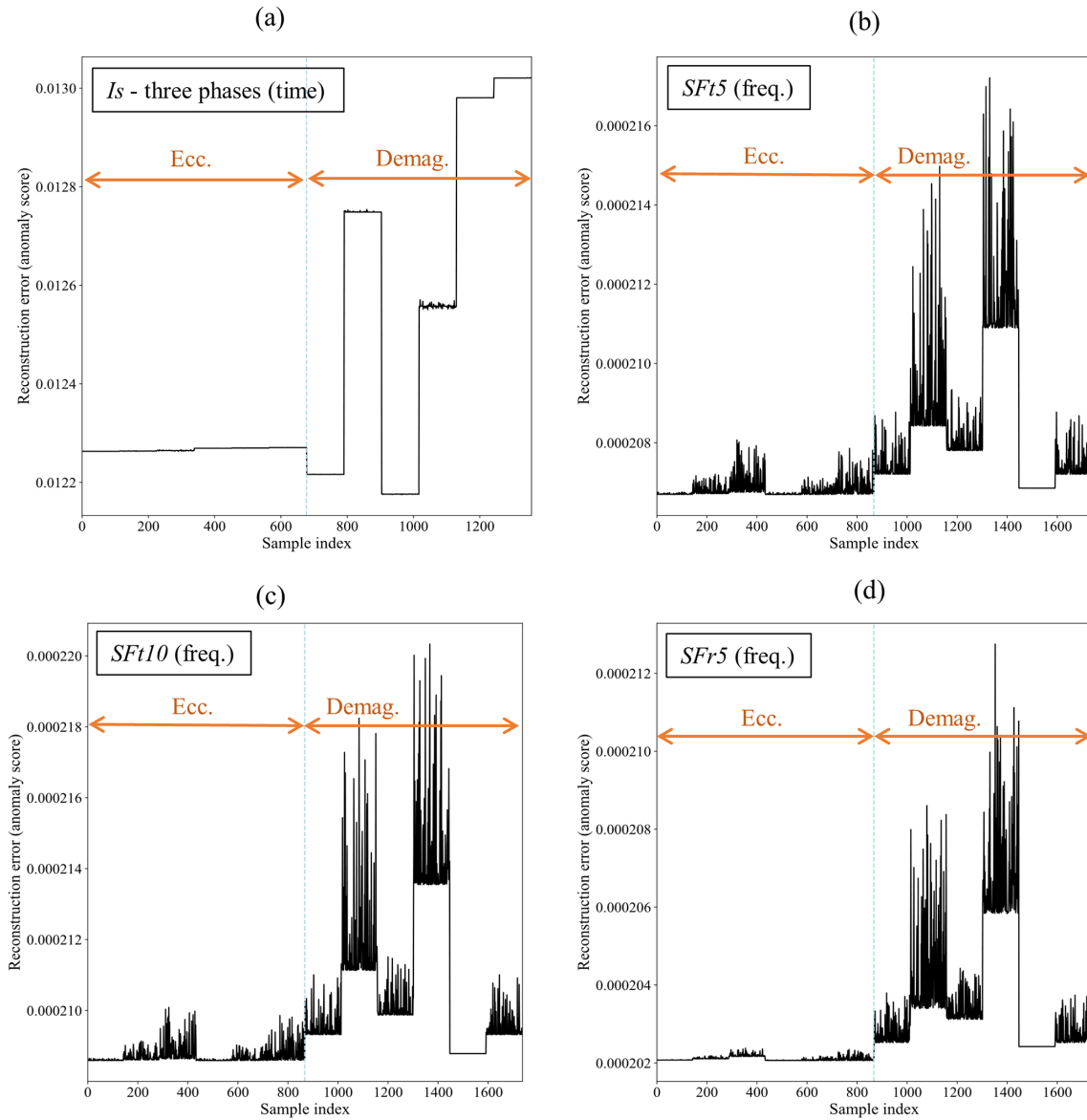
Figure 16. Anomaly detection results for both eccentricity and demagnetization: **(a)** time domain Is (three phases), **(b)** frequency domain SFt5, **(c)** frequency domain SFt10, and **(d)** frequency domain SFr5.

Table 8. Comparison of performance metrics for anomaly detection models.

Metric	k-means model	KNN	One-class SVM	CAE (proposed)
F1 score	0.8361	0.8672	0.8878	1.0000
Accuracy (%)	85.5	85.0	88.0	100.0

5 Conclusions

This study has successfully demonstrated the application of convolutional autoencoder (CAE) models for anomaly detection in offshore wind permanent-magnet synchronous generators (PMSGs), addressing demagnetization and eccentricity faults of varying severity. Utilizing a simulation high-speed PMSG model design based on the specifications of the NREL 5 MW reference offshore wind turbine, this research employed unsupervised CAE models trained on healthy-state simulation data to analyze a range of signals, including three-phase currents, induced shaft voltage, electromagnetic torque, and air gap and stray magnetic flux. While

Figure 17. Confusion matrices for performance evaluation across different anomaly detection models trained with time-domain data of three-phase stator current measurements.

some of these measurements, such as phase currents, are typically included in the supervisory control and data acquisition (SCADA) systems of wind turbines, they are often at a low resolution. A key limitation of these downsampled data is their inability to detect emerging failures in PMSGs as promptly as necessary. Hence, this study aimed to evaluate the potential of high-resolution measurements for the early detection of possible failures in PMSGs. The findings indicate that three-phase currents in the time domain, along with a combination of top, bottom, and side positions of stray flux sensors – both tangential and radial components in the frequency domain – significantly enhance anomaly detection accuracy and fault severity sensitivity. Notably, the radial components of stray flux sensors proved capable of differentiating between types of eccentricity and demagnetization faults. The findings suggest that using flux monitoring techniques, with cost-efficient and easily installed stray flux sen-

sors with frequency information, could be an effective strategy for early fault detection in large MW offshore wind generators. Future work will focus on further validating these results with experimental data and exploring the impact of varying measurement resolutions to determine the minimum resolution necessary for early fault detection, thereby confirming the models' effectiveness in practical scenarios.

References

Ágoston, K.: Fault Detection of the Electrical Motors Based on Vibration Analysis, 8th International Conference Interdisciplinarity in Engineering, INTER-ENG 2014, 9–10 October 2014, Tirgu Mures, Romania, Proc. Tech., 19, 547–553, https://doi.org/10.1016/j.protcy.2015.02.078, 2015.

Ali, M. Z., Shabbir, M. N. S. K., Liang, X., Zhang, Y., and Hu, T.: Machine learning-based fault diagnosis for single- and multi-faults in induction motors using measured stator currents and vibration signals, IEEE T. Ind. Appl., 55, 2378–2391, https://doi.org/10.1109/TIA.2019.2895797, 2019.

Bernier, S., Merkhouf, A., and Al-Haddad, K.: Stray flux and air gap flux experimental measurement and analysis in large hydro generators, Proceedings – 2023 IEEE Workshop on Electrical Machines Design, Control and Diagnosis, WEMDCD 2023, Newcastle upon Tyne, England, 13–14 April 2023, 1–6, https://doi.org/10.1109/WEMDCD55819.2023.10110944, 2023.

Borchersen, A. B. and Kinnaert, M.: Model-based fault detection for generator cooling system in wind turbines using SCADA data, Wind Energy, 19, 593–606, 2016.

Cai, B., Hao, K., Wang, Z., Yang, C., Kong, X., Liu, Z., Ji, R., and Liu, Y.: Data-driven early fault diagnostic methodology of permanent magnet synchronous motor, Expert Syst. Appl., 177, 115000, https://doi.org/10.1016/j.eswa.2021.115000, 2021.

Campoverde-Vilela, L., Feijóo, M. C., Vidal, Y., Sampietro, J., and Tutivén, C.: Anomaly-based fault detection in wind turbine main bearings, Wind Energ. Sci., 8, 557–574, https://doi.org/10.5194/wes-8-557-2023, 2023.

Carroll, J., McDonald, A., and McMillan, D.: Reliability Comparison of Wind Turbines With DFIG and PMG Drive Trains, IEEE T. Energy Conver., 30, 663–670, https://doi.org/10.1109/TEC.2014.2367243, 2015.

Chen, P., Li, Y., Wang, K., Zuo, M. J., Heyns, P. S., and Baggeröhr, S.: A threshold self-setting condition monitoring scheme for wind turbine generator bearings based on deep convolutional generative adversarial networks, Measurement, 167, 108234, https://doi.org/10.1016/j.measurement.2020.108234, 2021.

Choi, G.: Analysis and Experimental Verification of the Demagnetization Vulnerability in Various PM Synchronous Machine Configurations for an EV Application, Energies, 14, 5447, https://doi.org/10.3390/en14175447, 2021.

Choi, S., Haque, M. S., Tarek, M. T. B., Mulpuri, V., Duan, Y., Das, S., Garg, V., Ionel, D. M., Masrur, M. A., Mirafzal, B., and Toliyat, H. A.: Fault Diagnosis Techniques for Permanent Magnet AC Machine and Drives – A Review of Current State of the Art, IEEE Transactions on Transportation Electrification, 4, 444–463, https://doi.org/10.1109/TTE.2018.2819627, 2018.

Choudhary, A., Goyal, D., and Letha, S. S.: Infrared Thermography-Based Fault Diagnosis of Induction Motor Bearings Using Machine Learning, IEEE Sens. J., 21, 1727–1734, https://doi.org/10.1109/JSEN.2020.3015868, 2021.

Da, Y., Shi, X., and Krishnamurthy, M.: A New Approach to Fault Diagnostics for Permanent Magnet Synchronous Machines Using Electromagnetic Signature Analysis, IEEE T. Power Electr., 28, 4104–4112, https://doi.org/10.1109/TPEL.2012.2227808, 2013.

Dibaj, A., Nejad, A. R., and Gao, Z.: A data-driven approach for fault diagnosis of drivetrain system in a spar-type floating wind turbine based on the multi-point acceleration measurements, J. Phys. Conf. Ser., 2265, 032096, https://doi.org/10.1088/1742-6596/2265/3/032096, 2022.

Dibaj, A., Gao, Z., and Nejad, A. R.: Fault detection of offshore wind turbine drivetrains in different environmental conditions through optimal selection of vibration measurements, Renew. Energ., 203, 161–176, https://doi.org/10.1016/j.renene.2022.12.049, 2023.

Ding, X., Xu, J., Wang, J., and Zheng, J.: Fault diagnosis of wind turbine generator bearings using fast spectral correlation, Wind Engineering, 46, 724–736, https://doi.org/10.1177/0309524X211046381, 2022.

Ebrahimi, B. M., Faiz, J., and Roshtkhari, M. J.: Static-, dynamic-, and mixed-eccentricity fault diagnoses in permanent-magnet synchronous motors, IEEE T. Ind. Electron., 56, 4727–4739, https://doi.org/10.1109/TIE.2009.2029577, 2009.

Ebrahimi, B. M., Javan Roshtkhari, M., Faiz, J., and Khatami, S. V.: Advanced Eccentricity Fault Recognition in Permanent Magnet Synchronous Motors Using Stator Current Signature Analysis, IEEE T. Ind. Electron., 61, 2041–2052, https://doi.org/10.1109/TIE.2013.2263777, 2014.

Ebrahimi, M., Verij Kazemi, M., and Gholamian, S. A.: Detection of Partial Demagnetization Fault in Wind Turbine Permanent Magnet Generator Using a Data-Driven Method, Electr. Po. Compo. Sys., 50, 530–537, https://doi.org/10.1080/15325008.2022.2136789, 2022.

Ehya, H., Nysveen, A., and Antonino-Daviu, J. A.: Advanced Fault Detection of Synchronous Generators Using Stray Magnetic Field, IEEE T. Ind. Electron., 69, 11675–11685, https://doi.org/10.1109/TIE.2021.3118363, 2022a.

Ehya, H., Skreien, T. N., and Nysveen, A.: Intelligent Data-Driven Diagnosis of Incipient Interturn Short Circuit Fault in Field Winding of Salient Pole Synchronous Generators, IEEE T. Ind. Inform., 18, 3286–3294, https://doi.org/10.1109/TII.2021.3054674, 2022b.

Faiz, J. and Mazaheri-Tehrani, E.: Demagnetization Modeling and Fault Diagnosing Techniques in Permanent Magnet Machines Under Stationary and Nonstationary Conditions: An Overview, IEEE T. Ind. Appl., 53, 2772–2785, https://doi.org/10.1109/TIA.2016.2608950, 2017.

Freire, N. M. and Cardoso, A. J.: Fault detection and condition monitoring of pmsgs in offshore wind turbines, Machines, 9, 260, https://doi.org/10.3390/machines9110260, 2021.

Givnan, S., Chalmers, C., Fergus, P., Ortega-Martorell, S., and Whalley, T.: Anomaly detection using autoencoder reconstruction upon industrial motors, Sensors, 22, 3166, https://doi.org/10.3390/s22093166, 2022.

Goodfellow, I., Bengio, Y., and Courville, A.: Deep learning, MIT Press, ISBN 9780262035613, 2016.

GWEC: GWECs Global Offshore Wind Report 2022 – Global Wind Energy Council, https://gwec.net/gwecs-global-offshore-wind-report/ (last access: December 2023), 2022.

Gyftakis, K. N., Skarmoutsos, G. A., Barajas-Solano, I., Burchell, J., and Mueller, M.: Critical Aspects of Demagnetization Faults in Multi-Stage Direct Drive Permanent Magnet Generators for Renewables, IEEE T. Ind. Appl., 59, 6655–6663, https://doi.org/10.1109/TIA.2023.3299905, 2023.

Hoang Nguyen, N. D., Huynh, V. K., and Robbersmyr, K. G.: Current and Stray Flux Sensors for Anomaly Detection in PMSM Drive Based on Gradient Boosting Machine, P. IEEE Sensor., Vienna, Austria, 2023, 1–4, https://doi.org/10.1109/SENSORS56945.2023.10325076, 2023.

Huang, F., Zhang, X., Qin, G., Xie, J., Peng, J., Huang, S., Long, Z., and Tang, Y.: Demagnetization Fault Diagnosis of Permanent Magnet Synchronous Motors Using Magnetic Leakage Signals, IEEE T. Ind. Inform., 19, 6105–6116, https://doi.org/10.1109/TII.2022.3165283, 2023.

Jonkman, J., Butterfield, S., Musial, W., and Scott, G.: Definition of a 5-MW Reference Wind Turbine for Offshore System Development, National Renewable Energy Laboratory, https://doi.org/10.2172/947422, 2009.

Khanjani, M. and Ezoji, M.: Electrical fault detection in three-phase induction motor using deep network-based features of thermograms, Measurement, 173, 108622, https://doi.org/10.1016/j.measurement.2020.108622, 2021.

Kudelina, K., Asad, B., Vaimann, T., Rassõlkin, A., Kallaste, A., and Van Khang, H.: Methods of Condition Monitoring and Fault Detection for Electrical Machines, Energies, 14, 7459, https://doi.org/10.3390/EN14227459, 2021.

Lei, Y., Yang, B., Jiang, X., Jia, F., Li, N., and Nandi, A. K.: Applications of machine learning to machine fault diagnosis: A review and roadmap, Mech. Syst. Signal Pr., 138, 106587, https://doi.org/10.1016/j.ymssp.2019.106587, 2020.

Li, Y., Jiang, W., Zhang, G., and Shu, L.: Wind turbine fault diagnosis based on transfer learning and convolutional autoencoder with small-scale data, Renew. Energ., 171, 103–115, https://doi.org/10.1016/j.renene.2021.01.143, 2021.

Lopez-Perez, D. and Antonino-Daviu, J.: Application of infrared thermography to failure detection in industrial induction motors: case stories, IEEE T. Ind. Appl., 53, 1901–1908, 2017.

Lu, B., Dibaj, A., Gao, Z., Nejad, A. R., and Zhang, Y.: A class-imbalance-aware domain adaptation framework for fault diagnosis of wind turbine drivetrains under different environmental conditions, Ocean Eng., 296, 116902, https://doi.org/10.1016/j.oceaneng.2024.116902, 2024.

Mahmoud, M. S., Huynh, V. K., Sri, J., Senanyaka, L., and Robbersmyr, K. G.: Robust Multiple-Fault Diagnosis of PMSM Drives under Variant Operations and Noisy Conditions, IEEE Open Journal of the Industrial Electronics Society, 4, 762–772, https://doi.org/10.1109/OJIES.2024.3350443, 2024.

Mazaheri-Tehrani, E. and Faiz, J.: Airgap and stray magnetic flux monitoring techniques for fault diagnosis of electrical machines: An overview, IET Electr. Power App., 16, 277–299, https://doi.org/10.1049/elp2.12157, 2022.

Miele, E. S., Bonacina, F., and Corsini, A.: Deep anomaly detection in horizontal axis wind turbines using Graph Convolutional Autoencoders for Multivariate Time series, Energy and AI, 8, 100145, https://doi.org/10.1016/j.egyai.2022.100145, 2022.

Moghadam, F. K. and Nejad, A. R.: Evaluation of PMSG-based drivetrain technologies for 10-MW floating offshore wind turbines: Pros and cons in a life cycle perspective, Wind Energy, 23, 1542–1563, https://doi.org/10.1002/we.2499, 2020.

Nejad, A. R., Keller, J., Guo, Y., Sheng, S., Polinder, H., Watson, S., Dong, J., Qin, Z., Ebrahimi, A., Schelenz, R., Gutiérrez Guzmán, F., Cornel, D., Golafshan, R., Jacobs, G., Blockmans, B., Bosmans, J., Pluymers, B., Carroll, J., Koukoura, S., Hart, E., McDonald, A., Natarajan, A., Torsvik, J., Moghadam, F. K., Daems, P.-J., Verstraeten, T., Peeters, C., and Helsen, J.: Wind turbine drivetrains: state-of-the-art technologies and future development trends, Wind Energ. Sci., 7, 387–411, https://doi.org/10.5194/wes-7-387-2022, 2022.

Nyanteh, Y., Edrington, C., Srivastava, S., and Cartes, D.: Application of Artificial Intelligence to Real-Time Fault Detection in Permanent-Magnet Synchronous Machines, IEEE T. Ind. Appl., 49, 1205–1214, https://doi.org/10.1109/TIA.2013.2253081, 2013.

Ogidi, O. O., Barendse, P. S., and Khan, M. A.: Detection of Static Eccentricities in Axial-Flux Permanent-Magnet Machines With Concentrated Windings Using Vibration Analysis, IEEE T. Ind. Appl., 51, 4425–4434, https://doi.org/10.1109/TIA.2015.2448672, 2015.

Ortiz-Medina, R. A., Sanabria-Villamizar, M., Lopez-Garcia, I., Villalobos-Piña, F. J., Beltran-Carbajal, F., and Maldonado-Ruelas, V. A.: Wavelet and Hilbert Huang Transforms Applied to Park's Vector for Fault Detection in a PMSG Wind Turbine, 2023 IEEE 6th Colombian Conference on Automatic Control (CCAC), Popayan, Colombia, 17–20 October 2023, 1–6, https://doi.org/10.1109/ccac58200.2023.10333368, 2023.

Penrose, H. W.: Machine Learning for Electric Machine Prognostics and Remaining Useful Life with Basic Motor Data, in: 2022 IEEE Electrical Insulation Conference (EIC), Knoxville, TN, USA, 19–23 June 2022, https://doi.org/10.1109/EIC51169.2022.10122613, 245–248, 2022.

Peres, R. S., Jia, X., Lee, J., Sun, K., Colombo, A. W., and Barata, J.: Industrial Artificial Intelligence in Industry 4.0 – Systematic Review, Challenges and Outlook, IEEE Access, 8, 220121–220139, https://doi.org/10.1109/ACCESS.2020.3042874, 2020.

Qiu, Y., Feng, Y., Sun, J., Zhang, W., and Infield, D.: Applying thermophysics for wind turbine drivetrain fault diagnosis using SCADA data, IET Renew. Power Gen., 10, 661–668, https://doi.org/10.1049/iet-rpg.2015.0160, 2016.

Rousseeuw, P. J.: Silhouettes: A graphical aid to the interpretation and validation of cluster analysis, J. Comput. Appl. Math., 20, 53–65, https://doi.org/10.1016/0377-0427(87)90125-7, 1987.

Rumelhart, D. E., Hinton, G. E., and Williams, R. J.: Learning representations by back-propagating errors, Nature, 323, 533–536, https://doi.org/10.1038/323533a0, 1986.

Singh, G. and Sa'ad Ahmed, S. A. K.: Vibration signal analysis using wavelet transform for isolation and identification of electrical faults in induction machine, Electr. Pow. Syst. Res., 68, 119–136, https://doi.org/10.1016/S0378-7796(03)00154-8, 2004.

Stipetic, S., Kovacic, M., Hanic, Z., and Vrazic, M.: Measurement of Excitation Winding Temperature on Synchronous Generator in Rotation Using Infrared Thermography, IEEE T. Ind. Electron., 59, 2288–2298, https://doi.org/10.1109/TIE.2011.2158047, 2012.

Su, H. and Chong, K. T.: Induction machine condition monitoring using neural network modeling, IEEE T. Ind. Electron., 54, 241–249, https://doi.org/10.1109/TIE.2006.888786, 2007.

Su, H., Chong, K. T., and Ravi Kumar, R.: Vibration signal analysis for electrical fault detection of induction machine using neural networks, Neural Comput. Appl., 20, 183–194, 2011.

Tan, Y., Zhang, H., and Zhou, Y.: Fault Detection Method for Permanent Magnet Synchronous Generator Wind Energy Converters Using Correlation Features Among Three-phase Currents, J. Mod. Power Syst. Cle., 8, 168–178, https://doi.org/10.35833/MPCE.2018.000347, 2020.

Tong, W., Li, S., Pan, X., Wu, S., and Tang, R.: Analytical Model for Cogging Torque Calculation in Surface-Mounted Permanent Magnet Motors With Rotor Eccentricity and Magnet Defects, IEEE T. Energy Conver., 35, 2191–2200, https://doi.org/10.1109/TEC.2020.2995902, 2020.

Valavi, M., Nysveen, A., and Nilssen, R.: Analysis of a low-speed PM Wind generator with concentrated windings in eccentricity conditions, 2013 International Conference on Electrical Machines and Systems (ICEMS), Busan, Korea (South), 26–29 October 2013, https://doi.org/10.1109/ICEMS.2013.6713349, 1266–1270, 2013.

Valavi, M., Jorstad, K. G., and Nysveen, A.: Electromagnetic analysis and electrical signature-based detection of rotor inter-turn faults in salient-pole synchronous machine, IEEE T. Magn., 54, 8104309, https://doi.org/10.1109/TMAG.2018.2854670, 2018.

Wang, C., Liu, X., and Chen, Z.: Incipient Stator Insulation Fault Detection of Permanent Magnet Synchronous Wind Generators Based on Hilbert–Huang Transformation, IEEE T. Magn., 50, 1–4, https://doi.org/10.1109/TMAG.2014.2318207, 2014.

Wang, C., Delgado Prieto, M., Romeral, L., Chen, Z., Blaabjerg, F., and Liu, X.: Detection of Partial Demagnetization Fault in PMSMs Operating under Nonstationary Conditions, IEEE T. Magn., 52, 1–4, https://doi.org/10.1109/TMAG.2015.2511003, 2016.

Wang, Y., Yoshihashi, R., Kawakami, R., You, S., Harano, T., Ito, M., Komagome, K., Iida, M., and Naemura, T.: Unsupervised anomaly detection with compact deep features for wind turbine blade images taken by a drone, IPSJ Transactions on Computer Vision and Applications, 11, 0–6, https://doi.org/10.1186/s41074-019-0056-0, 2019.

Wu, X., Zhang, Y., Cheng, C., and Peng, Z.: A hybrid classification autoencoder for semi-supervised fault diagnosis in rotating machinery, Mech. Syst. Signal Pr., 149, 107327, https://doi.org/10.1016/j.ymssp.2020.107327, 2021.

Xiang, L., Yang, X., Hu, A., Su, H., and Wang, P.: Condition monitoring and anomaly detection of wind turbine based on cascaded and bidirectional deep learning networks, Appl. Energ., 305, 117925, https://doi.org/10.1016/j.apenergy.2021.117925, 2022.

Yang, W.: Condition monitoring and fault diagnosis of a wind turbine synchronous generator drive train, IET Renew. Power Gen., 3, 1–11, https://digital-library.theiet.org/content/journals/10.1049/iet-rpg_20080006 (last access: February 2024), 2009.

Zhang, J., Tounzi, A., Benabou, A., and Le Menach, Y.: Detection of magnetization loss in a PMSM with Hilbert Huang transform applied to non-invasive search coil voltage, Math. Comput. Simulat., 184, 184–195, https://doi.org/10.1016/j.matcom.2020.02.009, eLECTRIMACS 2019 ENGINEERING – Modelling and computational simulation for analysis and optimisation in electrical power engineering, 2021.

Zhao, Y., Li, D., Dong, A., Kang, D., Lv, Q., and Shang, L.: Fault prediction and diagnosis of wind turbine generators using SCADA data, Energies, 10, 1–17, https://doi.org/10.3390/en10081210, 2017.